Biophysical Journal
Article

Biophysical Society

Pulling, failing, and adaptive mechanotransduction of macrophage filopodia

Rebecca Michiels,[1] Nicole Gensch,[2] Birgit Erhard,[1] and Alexander Rohrbach[1,3,*]
[1]Laboratory for Bio- and Nano-Photonics, Department of Microsystems Engineering, University of Freiburg, Freiburg, Germany; [2]Core Facility Signalling Factory, University of Freiburg, Freiburg, Germany; and [3]CIBSS, Centre for Integrative Biological Signalling Studies, Freiburg, Germany

ABSTRACT Macrophages use filopodia to withdraw particles toward the cell body for phagocytosis. This can require substantial forces, which the cell generates after bio-mechanical stimuli are transmitted to the filopodium. Adaptation mechanisms to mechanical stimuli are essential for cells, but can a cell iteratively improve filopodia pulling? If so, the underlying mechanic adaptation principles organized on the protein level are unclear. Here, we tackle this problem using optically trapped 1 μm beads, which we tracked interferometrically at 1 MHz during connection to the tips of dorsal filopodia of macrophages. We observe repetitive failures while the filopodium tries to pull the bead out of the optical trap. Analyses of mean bead motions and position fluctuations on the nano-meter and microsecond scale indicate mechanical ruptures caused by a force-dependent actin-membrane connection. We found that beads are retracted three times slower under any load between 5 and 40 pN relative to the no-load transport, which has the same speed as the actin retrograde flow obtained from fluorescent speckle tracking. From this duty ratio of pulling velocities, we estimated a continuous on/off binding with $\tau_{off} = 2 \cdot \tau_{on}$, with measured off times $\tau_{off} = 0.1$–0.5 s. Remarkably, we see a gradual increase of filopodia pulling forces from 10 to 30 pN over time and after failures, which points toward an unknown adaptation mechanism. Additionally, we see that the attachment strength and friction between the bead and filopodium tip increases under load and over time. All observations are typical for catch-bond proteins such as integrin-talin complexes. We present a mechanistic picture of adaptive mechanotransduction, which formed by the help of mathematical models for repetitive tip ruptures and reconnections. The analytic mathematical model and the stochastic computer simulations, both based on catch-bond lifetimes, confirmed our measurements. Such catch-bond characteristics could also be important for other immune cells taking up counteracting pathogens.

SIGNIFICANCE Filopodia of macrophages catch and retract pathogens to clear pathogens in the body, -even against counteracting forces. The concepts of filopodia pulling at targets, rupturing, and reconnecting is of relevance for future nano-technological systems. Actin-related restructuring at the filopodia tips is so small and fast that common microscopy techniques are not good enough to uncover the underlying molecular processes. However, by microsecond probing the temporal changes of the particle's thermal motion, which is in contact with the filopodia tip, distinct nano-mechanical quantities can be extracted, providing a detailed mechanistic picture about the underlying biophysics. Remaining open questions are not answered by biochemical manipulation but by two independent mathematical models, which are based on catch-bond characteristics.

INTRODUCTION

Multicellular eukaryotic organisms such as animal species are able to adapt their forces to catch counteracting preys under different conditions. In a comparable way, single cells, which work as semi-autonomous units, are in constant physical and chemical interactions with their surroundings and hence must be able to adapt to environmental conditions with specific signaling pathways that trigger the cellular response (1,2). One important type of external signals transmitted to cells are mechanical cues (3,4). Specialized leukocytes, such as macrophages, possess abundant filopodia that continuously sense and process different external biochemical and mechanical stimuli. Mechanical sensing is mediated through the filopodia tips, which can pull pathogens toward the cell body with variable forces. Although filopodia are slender, isolated cellular structures, they exert comparably high

Submitted April 11, 2022, and accepted for publication July 21, 2022.
*Correspondence: rohrbach@imtek.de
Editor: Timo Betz.
https://doi.org/10.1016/j.bpj.2022.07.028
© 2022 Biophysical Society.

forces and possibly are mechano-adaptative under load to maintain their function.

When macrophage cells use filopodia to catch pathogens as a preparation for phagocytic uptake, they usually pull the attached particles toward the cell body by dynamic dorsal filopodia. But even with static, adherent filopodia, particles are transported along filopodia in a surfing-like manner and are later taken up and digested (5–7). The withdrawal process constitutes an important element of the immune response and enhances the efficiency of macrophage cells in eliminating pathogens. In order to retract particles successfully, filopodia must be able to form stable attachments and to exert considerable forces, especially relevant in the context of motile opposing targets like living bacteria. Another optical-tweezers-based study found that HeLa filopodia are limited in their capability to retract against counteracting forces in the pN range and that reversible actin tethering at the tip controls force transduction (8). Macrophage filopodia have been seen to overcome considerably larger forces (5,6). Using mainly physics methods, our study investigates which elements of filopodia crucially limit force transduction in macrophages and whether macrophage cells react to opposing motile pathogens by mechanical adaptation.

For many mechanosensitive processes, the actin cytoskeleton is believed to be crucial for signal transmission and subsequent cellular action. Filopodia contain a core of actin filaments, which are arranged in parallel bundles and form the backbone of filopodia, which ensures mechanical stability (9). The actin filaments inside the filopodium are shifted toward the cell body in a constant rearward movement termed "retrograde flow" (10). This movement originates mainly from two characteristic processes. The first is the inward push of actin monomers, which polymerize at the actin tip (11) with help of formins (12). Second, myosin II motors in the cell cortex (where filopodia are emanating from the actin network) contribute to retrograde flow in filopodia and lamellipodia by constant pulling (13). A recent study (12) showed that beads unbind from filopodia tips when the backbone pulling force releases, e.g., by myosin II depletion. At the tip of filopodia, several adhesion proteins are enriched, which can interact with the actin network via intermediate proteins such as talin. In macrophages, particularly immune receptors like FcR or integrin complement receptors are expressed. Integrins seems to transported toward filopodia tips by myosin X (14–16), which is possibly also involved in the attachment of pathogens (17). Best known from focal adhesions, the mechano-sensitive transmembrane protein integrin (18,19) binds to the long and slender protein talin, where both proteins switch between active and inactive states (17,20). Integrin connects through talin and the protein vinculin to the actin fibers (20,21), which together define the viscoelastic properties of focal adhesions or possibly also of filopodia tips.

In this study we want to answer the question how mechanosensitive adhesion proteins can organize mechanotransduction and force adaptation during filopodia pulling.

Our study is organized as follows: first, we show how to measure mean adaptive forces and binding strengths from fluctuating particles, which are visco-elastically attached to the tip of filopodia and which we control and track in position with a photonic force microscope. The three-dimensional (3D) position traces allow us to obtain relevant molecular binding parameters at the connection between the filopodium tip and the bead surface. These parameters are set in relation to fluorescence data to estimate on-/off-binding times of the bead to the actin backbone. In addition, we show that the binding parameters depend on the pulling strength of the filopodium. We demonstrate and quantify ruptures and rebindings at the filopodium tip upon exceedingly strong counteracting forces. We show that an adaptation of the bond formation at the tip and the pulling forces occurs over time. The observation of repetitive failures together with an overall increase in pulling force are confirmed by a nano-mechanical, mathematical model. See also Video S1.

MATERIALS AND METHODS

Cell preparation

J774 mouse macrophages (ATCC TIB-67, Manassas, VA, USA www.atcc.org/cell-products) transfected with pLife Act-TagGFP2 (ibidi GmbH, Gräfelfing, Germany) were cultured in Dulbecco's modified Eagle medium (GlutaMAX, Invitrogen Life Technologies, Carlsbad, CA, USA) and in a 37°C and 5% CO_2 atmosphere until the desired cell density for the experiments was reached (approx. 30% confluency). This cell line tested negative for mycoplasma. J774 cells are rich of FcγRs and complement and integrin receptors (22). The adherent cells are provided on microscope coverslips, which have been sterilized by an autoclave prior to cell preparation. All experiments were performed at 37°C temperature in buffer medium with 10% fetal bovine serum (containing also fibronectin) to provide nutrients and ensure near-physiological conditions. One μm sized carboxylate polystyrene beads (catalog number #08226, Polysciences, Warrington, PA, USA) were added to the medium at the start of each experiment.

Microscopy

We use differential interference contrast microscopy with a 1.2 numerical aperture (NA) objective lens (C-Apochromat 63×/1.20W Corr M27, Carl Zeiss, Jena, Germany) providing 320 nm lateral spatial resolution at high contrast to reveal the smallest structures, such as filopodia, at the cell periphery. Incoherent, low-power illumination with a white LED and a sensitive sCMOS camera (Hamamatsu ORCA Flash4.0 v.2, Hamamatsu, Japan) allows fast imaging at minimal phototoxicity.

We use photonic force microscopy to record and analyze the diffusive behavior of a bead in the vicinity of cells with nano-meter precision on a MHz spectral bandwidth. This is illustrated in Fig. 1. Here, the same 1.2 NA objective lens creates a tightly focused beam from a near-infrared laser (2W Nd:GdVO4 solid-state laser, Smart Laser Systems, Berlin, Germany), which constitutes the optical trap for the 1 μm beads used in this study. The incident electric field interferes with the fields scattered at the bead and at the cell. Two quadrant photo diodes (QPDs) located in the back focal plane of the detection lens (W Plan-Apochromat 63×/NA_{det} = 1.0, Carl Zeiss)

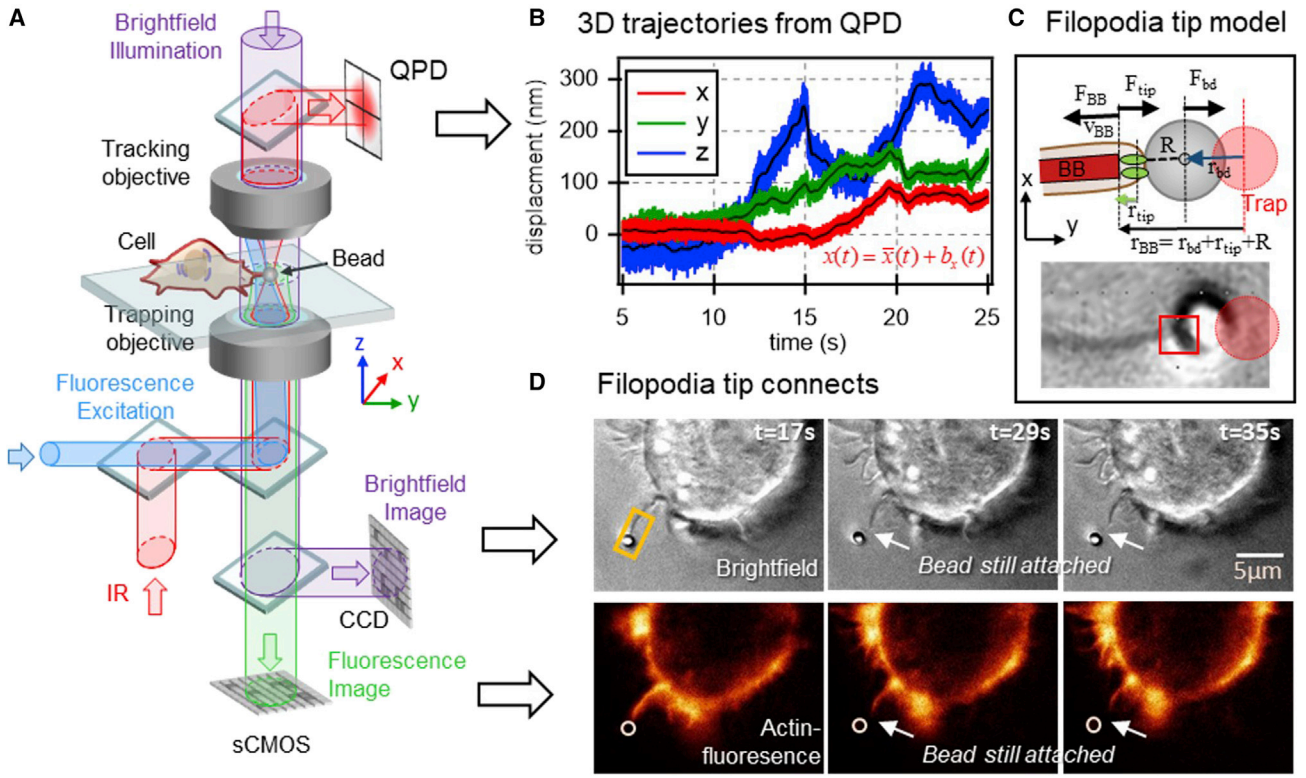

FIGURE 1 Microscope setup and data acquisition. (*A*) Sketch of optical setup with beam path for laser trapping and tracking (*red*), fluorescence imaging (*blue*/*green*), and bright-field imaging (*purple*). (*B*) The optically trapped bead moves within the trap potential by 0.15 µm in *x* and *y* and 0.3 µm in *z* directions, driven by thermal noise and forces of the filopodium tip. The fluctuation dominated bead trajectories in *x*, *y*, and *z* are recorded at 1 MHz by two QPDs and are used to analyze the bead interactions. (*C*) Sketch indicating counteracting optical and filopodial forces during retraction through the actin backbone (BB). The inset shows a magnified filopodia tip region from *D* (*orange frame*). (*D*) Bright-field and fluorescence images of LifeAct GFP J774 cells during retraction of the filopodium, which is connected to the bead at all three time points (see white arrows). Bright-field and fluorescence images are acquired simultaneously with two cameras. To see this figure in color, go online.

with different sensitivities record these voltage signals, which are then converted into the transversal bead displacements $b_x(t)$ and $b_y(t)$ (QPD1) and the axial bead displacement $b_z(t)$ (QPD2), respectively.

RESULTS

Microscopy, optical tweezing, and position tracking

We use an experimental approach in which we combine photonic force microscopy (5,23) and fluorescence microscopy as depicted in Fig. 1 *A*. An optical trap is formed by a stabilized, highly focused 1064 nm near-infrared laser. The optical trap is used to hold 1 µm carboxylated, but otherwise uncoated, polystyrene beads and present them to J774 macrophage cells as artificial pathogens. Polystyrene beads are opsonized by various molecules of the cell medium including fibronectin and have been successfully used as artificial phagocytic models systems to induce filopodia retraction in previous studies (5–7). Using interferometric particle tracking via two QPDs, the trajectory of the bead can be followed with nm precision on a MHz timescale as depicted in Fig. 1 *B*. Analysis of the probe's position mean values and fluctuations allows us to investigate the transport and binding of the bead with unmatched spatiotemporal precision and to extract the stiffness and friction parameters (see Eq. 1), which describe the viscoelastic properties of the surroundings of the bead. These parameters can be used to characterize mechanical properties of the attachment between bead and filopodium. The sample is concurrently imaged with low-power bright-field microscopy at a wavelength of 430 nm and fluorescence microscopy using a 491 nm laser for excitation of GFP fluorescence. Fluorescence can be excited either by illuminating the sample homogenously or by using a strongly inclined and focused laser to illuminate only structures of interest and to reduce out-of-focus blur (Fig. 1 *A*, *blue beam*). The tracking data are combined with time-lapse movies of both the whole cell in bright-field images and labeled cellular structures like the actin cytoskeleton in fluorescence images as shown in Fig. 1 *D*. Although in both imaging modes the filopodium directed to the bead can be well recognized, the direct connection between tip and bead is invisible. However, the bead's position fluctuations allowed us to identify the change in the tip connection precisely.

MHz-rate QPD tracking allows us to measure the bead's center position $r_j(t) = \bar{r}_j(t) + b_j(t)$ in directions $j = x, y, z$

on all timescales. The strategy in this article is to, on the one hand, analyze mean bead motions $\overline{r}_j(t)$ and forces on long-term timescales $t \gg t_{L(ong)}$ to describe transport and filopodia failing (Fig. 1 *B*, *black traces*). On the other hand, position fluctuations $b_j(t)$ and thermal forces $\mathbf{F}_{\mathrm{th}}$ provide information about the bond strength between the filopodium tip and the bead on short timescales $t < t_L$. This is indicated in Fig. 1 *B*, where colored traces indicate $r_j(t) = \overline{r}_j(t) + b_j(t)$ and the low-pass filtered traces $\overline{r}_j(t)$ are shown in black. The averaging time $t_L \approx 5$ ms is about 10 times as long as the bead's longest relaxation time in the stationary optical trap at position $\overline{\mathbf{r}} = 0$.

In our optical tweezers experiments, a bead of radius R experiences a tug of war between the optical trapping force on the bead $\mathbf{F}_{\mathrm{bd}}$, the filopodium tip connecting force $\mathbf{F}_{\mathrm{tip}}$, and the cellular retraction force $\mathbf{F}_{\mathrm{BB}}$. As shown in Fig. 1 *B*, the backbone (end) position $\mathbf{r}_{BB}(t) = \mathbf{r}_{bd}(t) + \mathbf{r}_0(t)$ (with $\mathbf{r}_0(t) = \mathbf{r}_{tip}(t) + \mathbf{R}$) increases with the bead displacement $\mathbf{r}_{bd}(t)$ and with the elongation $\mathbf{r}_{tip}(t)$ of a "molecular spring" at the tip.

viscosity η). The tip force $\mathbf{F}_{tip}(t) = (\gamma_{tip}(t) \cdot \mathbf{v}_{bd}(t)) + (\kappa_{tip}(t) \cdot \mathbf{r}_{bd}(t))$ varies in time not only with $\mathbf{r}_{bd}(t)$ but also with the friction $\gamma_{tip}(t)$ and elasticity $\kappa_{tip}(t)$ at the tip. This connection between the filopodium tip and the bead surface follows complicated mechanisms, which we want to unravel in this study.

Motion on short timescales $t \ll t_L$

Here, we assume that a BB moving slowly relative to the thermal position fluctuations, i.e., on short timescales $t << t_L \approx 5$ ms, the bead transport is negligible ($v_{BB} = \frac{\partial}{\partial t} r_{BB} < \frac{300nm}{s} = \frac{1.5nm}{t_L} \approx 0$). In this case, Eq. 1 corresponds to a parallel connection of damped springs prestressed with $F_{BB}(t_0)$. From the force equality $F_{bd}(\mathbf{r}_{bd}, t) = F_{tip}(\mathbf{r}_{tip}, t)$, we find $(\kappa_{opt} + \gamma_{bd}\frac{\partial}{\partial t}) r_{bd} + F_{th}(t) = (\kappa_{tip} + \gamma_{tip}\frac{\partial}{\partial t})(r_{BB} - R - r_{bd})$, which results in the following Langevin equation of motion for a fixed pulling distance $\mathbf{r}_{BB}$ and pulling force $F_{BB}(t_0) = \kappa_{tip}(\mathbf{r}_{BB}(t_0) - R)$ with $\gamma_{tip}\frac{\partial}{\partial t}(r_{BB} - R) = 0$:

$$
\begin{aligned}
t \ll t_L: \quad & (\kappa_{opt} + \kappa_{tip}) r_{bd} + (\gamma_{bd} + \gamma_{tip}) \frac{\partial}{\partial t} r_{bd} - F_{BB}(t_0) = -F_{th}(t) \\
t > t_L: \quad & \left(1/\kappa_{opt} + 1/\kappa_{tip}\right)^{-1} \cdot \overline{r}_{bd} - F_{BB}(\overline{r}_{bd}(t_0)) \approx 0.
\end{aligned}
\tag{1}
$$

Description of forces and motions

We need a mechanistic model to interpret and understand the measurement results. To test the mechanistic model for correctness, we developed the following mathematical model, expressed by equations of forces, motions, and mechanical parameters. Nearly every figure is described and explained in more detail by an equation, containing parameters from the figure.

The most relevant forces, describing the bead motions at the filopodium tip (which we can measure), are the pulling force of the backbone (BB) F_{BB}, the forces acting on the bead F_{bd}, including the thermal force F_{th}, and the forces F_{tip} acting on the tip connection. As illustrated in Fig. 1 *C*, the pulling force F_{BB} acts on viscoelastic structures coupled in series such that the displacement of the BB end $\mathbf{r}_{BB}(t) = \mathbf{r}_{tip}(t) + \mathbf{r}_{bd}(t) + \mathbf{R}$ splits up in the stretching $\mathbf{r}_{tip}$ of the tip bonds and the displacement $\mathbf{r}_{bd}$ of the bead (radius R) from the trap center.

In a serial connection, the resulting force is the same in all elements, i.e., $F_{BB}(\mathbf{r}_{BB}) = F_{bd}(\mathbf{r}_{bd}) = F_{tip}(\mathbf{r}_{tip})$. The force on a trapped bead $F_{bd}(\mathbf{r}_{bd}) = \mathbf{F}_{opt}(t) = \kappa_{opt} \cdot \mathbf{r}_{bd}(t) + \gamma_{bd} \cdot \frac{\partial}{\partial t}\mathbf{r}_{bd}(t)$ is the sum of the optical force and the friction force, which depends on the bead transport velocity $\mathbf{v}_{bd}(t) = \dot{\mathbf{r}}_{bd}(t)$ and where $\gamma_{bd} = 6\pi\eta R$ (at surrounding fluid

Motion on longer timescales $t > t_L$

By averaging all motions over the time t_L, fluctuations can be neglected. The average pulling velocity of the BB $\frac{1}{t_L}\int \dot{r}_{BB} dt = \overline{v}_{BB}$, is driven by myosin II motors (Fig. 1 *C*) and results in a mean pulling force $F_{BB}(\overline{r}_{BB}(t_0))$ at a given time point t_0. This situation corresponds to a serial arrangement of damped springs with κ_{tip} and κ_{opt}, where their displacements add up after the system nearly equilibrates such that the stiffnesses approximately add up inversely, i.e., $\kappa_{sum}^{-1} = \kappa_{tip}^{-1} + \kappa_{opt}^{-1}$.

Under load, bead transport becomes three times slower than actin retrograde flow

Here, we investigate the link between bead retraction and actin retrograde flow using J774 macrophages stably transfected with actin-EGFP. The actin-EGFP monomers are incorporated into filaments, but due to stochastic variations, their distribution along filaments vary and lead to bright or dark sections along the filaments. These EGFP "speckles" can be tracked in time-lapse movies as they move together with the actin BB at velocity $v_{BB}(t)$. To enable the tracking of speckles, the filopodium of interest is locally excited with a highly inclined laser beam of 491 nm wavelength,

illuminating an area of only 5 × 5 μm in the plane of the filopodium. The configuration illustrated in Fig. 2 *A* prevents strong out-of-focus blur, hence ensuring a sufficient signal-to-noise ratio to identify speckles in dorsal filopodia far away from the coverslip. With a dual-path imaging unit (see Fig. 1), we measure bright-field and fluorescence in parallel to directly compare bead and actin velocities. The velocities of the bead $v_{bd}(t)$ and of the BB EGFP-speckle $v_{BB}(t)$ (see Fig. 2 *A* and *B*) are obtained by fitting lines to kymographs of time-lapse movies as depicted in Figs. 2 *C* and S2.

When the optical trap is switched off ($F_{opt} = 0$) after the bead connects to a filopodium, only bead drag forces counteract the pulling force F_{BB} (zero-load case). For 1 μm beads in aqueous solution, the drag force in our experiments is approximately $F_{\gamma b} \approx 1$ fN at $v_{bd} = 0.15$ μm/s and, therefore, is orders of magnitude lower than the trap forces. In the case without loading force, the measured BB velocities vary between 100 and 270 nm/s in different experiments but are always strongly correlated with the measured bead velocity (Fig. 2 *D* and *E*, *blue markers*). The average actin retrograde flow velocity from 15 retractions is $v_{BB} = 173 \pm 69$ nm/s, and the average bead velocity is $v_{bd} = 153 \pm 64$ nm/s. Beads are never transported faster than the movement of the actin filaments and are, on average, 12% slower (see Eq. 2). In this zero-load case ($F_{opt} = 0$), all blue dots are found close to the dashed line, indicating approximately equal velocities $v_{BB} \approx v_{bd}$ (see Fig. 2 *E*). Beads and actin filaments always move toward the cell body (minus end), never away from it. A similar relationship predicted by a catch-bond cluster theory (which will be explained in a later section) is shown in the same figure, where the ratio $Q = v_{bd}/v_{BB}$ of bead velocity and BB velocity is always smaller than 1 (see bead velocities under load shown by red dots below dashed line $v_{bd} = v_{BB}$).

To retract optically trapped beads presented to the cell, filopodia pulled with forces in the range of $F_{BB} = 1$–40

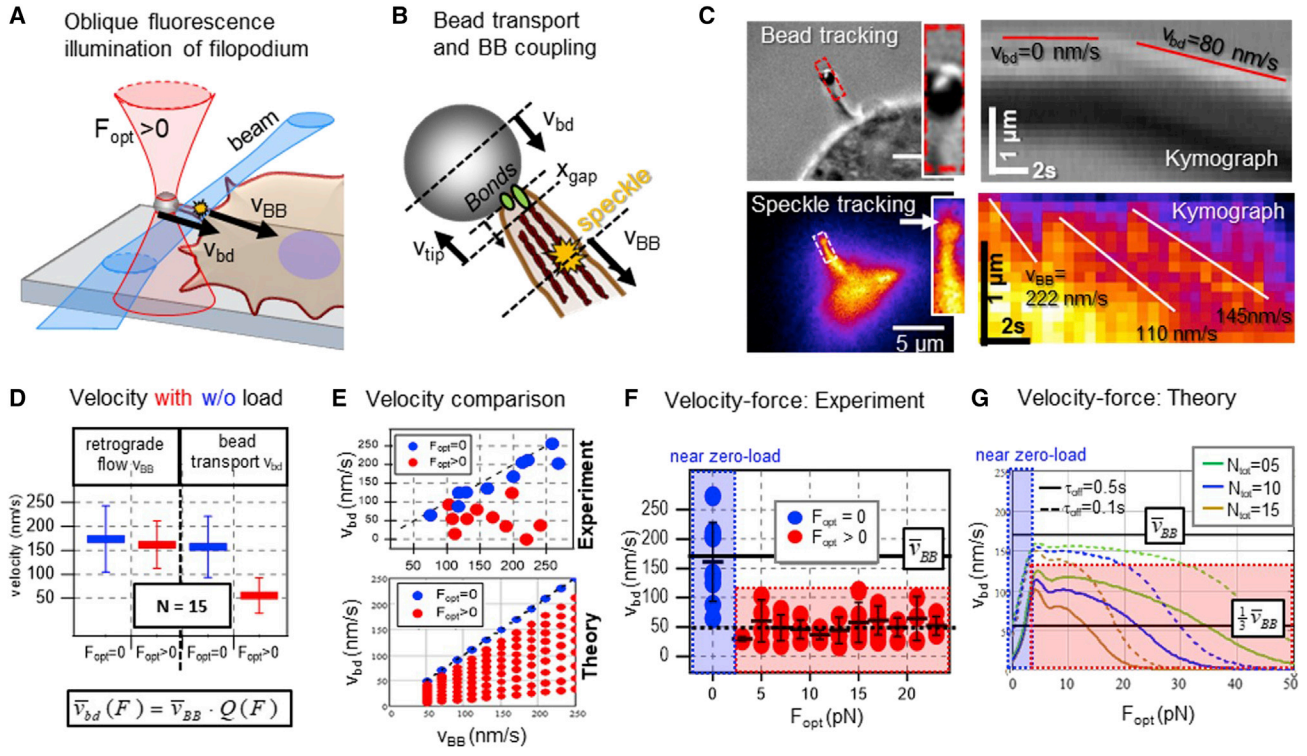

FIGURE 2 Analysis of actin speckle in actin-EGFP J774 cells and correlation with bead velocity during retraction. (*A*) Sketch of the measurement principle. The focused laser beam is tilted such that only the filopodium is illuminated with a limited depth of field. (*B*) Scheme illustrating the bead transport velocity relative to actin velocity and BB polymerization velocity over the tip gap length x_{gap}. (*C*) Bead motion (bright-field image) relative to actin speckle motion (fluorescence image). Kymographs of time-lapse movies of bead and fluorescently labeled filopodium BB during one pulling event are averaged in space within the dashed rectangular regions of interest. The kymograph through the fluorescent filopodium shows a moving signal edge (see *white arrow*), of which the velocity is determined. The actin retrograde flow is faster than the bead movement, indicating partial coupling with a duty ratio *Q*. (*D*) Average speed of actin retrograde flow and bead transport with (*red*) and without (*blue*) optical loading force. Vertical error bars are STDs. (*E*) Relationship between bead velocity and BB velocity determined from speckle analysis and from theory. Beads never move faster than the actin retrograde flow but slow down about threefold under force load. (*F*) Measured bead velocities are 50–270 nm/s at nearly-zero load ($F_{opt} < 4$ pN, *blue shaded area*) and decreased to 10–100 nm/s depending on the loading/pulling force ($F_{opt} > 4$ pN, *red shaded area*). Vertical error bars are STDs, horizontal error bars are pooled data. (*G*) Velocity-force relationship based on a catch-bond cluster model for three different bond numbers N_{tot} and two off-binding times τ_{off}. For nearly-zero-load forces (*blue shaded area*) bead velocities can reach the BB velocity v_{BB}. With increasing loading forces ($F_{opt} > 5$pN, *red shaded area*), velocities v_{bd} decay differently fast to below 100 nm/s depending on N_{tot} and τ_{off}. To see this figure in color, go online.

pN. Fig. 2 *D–F* demonstrate that bead transport is load dependent since already forces in the low pN range slow the bead down considerably, to an average velocity of $v_{bd} = 55 \pm 36$ nm/s, which is only about 1/3 of the average velocity of free beads. The optical force depends on the displacement of the bead from the trap center; therefore, the counteracting force is not constant during experiments in which the filopodium withdraws the bead from the trap. However, analysis of tracking data showed that the bead velocity is not directly correlated to the optical forces in the range that we analyze (Figs. 2 *F* and S1); therefore, all speckle tracking data were evaluated together. Remarkably, the mean actin retrograde flow velocity $v_{BB} \approx 160$ nm/s is nearly independent of the reduced bead velocity under load (see also Fig. S2). Fig. 2 *F* summarizes the experimental results, where the bead velocities in the zero-load case (blue shaded area) can be as high as the BB velocities but is instantly reduced to about $\overline{v}_{bd}/\overline{v}_{BB} \approx 1/3$, on average, when the loading force F_{opt} becomes larger than 3 pN.

Velocities of bead and BB are different: The model

On timescales of some 10 ms ($t \gg t_L$), continuous, not resolvable linker detachments of the BB from the membrane ($\overline{F}_{BB} \to 0$) occur with a mean off time τ_{off} relative to a mean on time τ_{on}. This leads to an average $\overline{v}_{bd}$, which is the measurable BB velocity $\overline{v}_{BB}$ multiplied by the transport duty ratio $Q_T = \tau_{on}/(\tau_{on} + \tau_{off}) < 1$ (see Fig. 2). The on time $\tau_{on}(F)$ reduces under force F (see Eq. 5), i.e., when the BB tip is in contact with the filopodia membrane before detachment. The time τ_{off} after detachment of the BB tip depends on how fast the BB tip increases in length at mean velocity $\overline{v}_{tip}$ to close the gap of length x_{gap}, i.e., $\tau_{off} = x_{gap}/\overline{v}_{tip}$. The velocity of the tip of the retracting BB $\overline{v}_{tip} = \overline{v}_{poly} - \overline{v}_{BB}$ is the polymerization speed $\overline{v}_{poly}$ reduced by the constant retrograde flow velocity $\overline{v}_{BB}$ of the BB. Hence, the measured mean bead retraction velocity $\overline{v}_{bd}(F) = \overline{v}_{BB} \cdot Q_T(F)$ can be expressed as

$$\begin{aligned} \overline{v}_{bd}(F) &= \overline{v}_{BB} \cdot \frac{\tau_{on}(F)}{\tau_{on}(F) + \tau_{off}} \\ &= \overline{v}_{BB} \cdot \frac{\tau_{on}(F)}{\tau_{on}(F) + x_{gap}/\overline{v}_{tip}}. \end{aligned} \tag{2}$$

As shown in Fig. 2 *D* and *E*, we find equal velocities of bead and actin BB for zero-force load F_{opt}, i.e., we have $\overline{v}_{bd}(F = 0) = \overline{v}_{BB}$ (with $Q_T = 1$ and $\tau_{off} = 0$). However, under force load, we observe a reduction of the bead retraction speed by a factor of $\frac{\overline{v}_{BB}}{\overline{v}_{bd}(F>0)} = 1 + \frac{\tau_{off}}{\tau_{on}(F>0)} \approx \frac{3}{1}$ relative to the load-free case, i.e., based on Eq. 2, we find that the averaged off time is twice the averaged on time, $\tau_{off} \approx 2 \cdot \langle \tau_{on}(F > 0) \rangle$. The tip velocity v_{tip} might depend on the force load as well, such that $\tau_{off}(F) = x_{gap}/\overline{v}_{tip}(F)$ (see section S7 of the supporting material). Fig. 2 *F* and *G* illustrate Eq. 2, where we used $\tau_{on}(F) = \tau_{fail}(F, N)$ from Eq. 5.

A mean lifetime τ_{on} of a few 100 ms at a load force of a few pN in actin plus end direction has been reported (24) for the actin linker molecule talin as part of a catch-slip bond pair with the integrin receptor. This maximum force at a 0.5 s lifetime has been used for the calculated velocity force relations in Fig. 2 *G*, where a cluster of totally N_{tot} bonds are most stable for low forces $F_{opt} < 5$ pN, leading to high bead velocities (blue shaded area). For $F_{opt} > 5$ pN, the velocities decay quickly below $v_{bd} < 100$ nm/s depending on N_{tot} and τ_{off} (within the red shaded region), which coincides well with the experimental results.

Bead fluctuations decrease during filopodia binding and pulling

Neither fluorescence nor differential interference contrast microscopy allows us to decipher the processes at the filopodium tip, as shown by the two snapshots at $t = 33.5$ and 36.5 s in Fig. 3 *A* (see arrows). The tip connection factors κ_{tip} and γ_{tip} for stiffness and friction can only be extracted from high-frequency fluctuation data (Fig. 3 *B* and *D*). Fig. 3 *B* depicts exemplarily two exponential decays of the autocorrelation function AC[$b_x(t)$] analyzed within a time window of $dt = 5$ ms prior to and after connection of the filopodium based on Eq. 3. While AC(0) provides κ, the slope of AC(τ) provides γ at arbitrary time points t. By interferometric tracking of the bead fluctuations close to the filopodia tips, we measured both the change in the mean bead displacements $\overline{\mathbf{r}}(t)$ and in the position fluctuations $\mathbf{b}(t)$ during binding, as illustrated in Fig. 3 *C*. Here, $\overline{r}_{\perp}(t)$ and $\overline{r}_{\parallel}(t)$ are the lateral and radial displacements within ± 70 nm (in green and red, respectively), which are proportional to the loading force of the BB retraction $F_{BB}(t) = F_{opt}(t)$, corresponding to 7 pN at maximum. Although changes in fluctuation width are hardly visible in the top plot of Fig. 3 *C*, AC fluctuation analysis reveals distinct and typical changes in bond stiffness $\kappa_{tip}(t)$ and the measured friction parameter $\gamma_{tip}(t)$ at the filopodia tips (see Eq. 3). Prior to connection to the filopodium tip (see dark red arrow at $t_1 = 33$s), the fluctuation behavior is defined by the optical trap, and no directional dependency is visible, such that $\kappa_{\parallel} \approx \kappa_{\perp}$ and $\gamma_{\parallel} \approx \gamma_{\perp}$. However, upon connection to the tip, both values of κ_{tip} and γ_{tip} increase manyfold within less than a second at about $t_L = 34.5$ s, as indicated by the orange and blue arrow in the two graphs. The corresponding sketches in Fig. 3 *C* indicate the changes in fluctuation widths by the lateral green and radial red double arrows. Two seconds later, at $t_2 = 36.5$s (blue arrow), both mean bead displacement and loading force increase significantly, while fluctuation widths and their autocorrelation times decrease significantly in the radial direction, meaning that the tip connection becomes stiffer and more viscous, i.e., that $\kappa_{\parallel} \gg \kappa_{\perp}$ and $\gamma_{\parallel} \gg \gamma_{\perp}$.

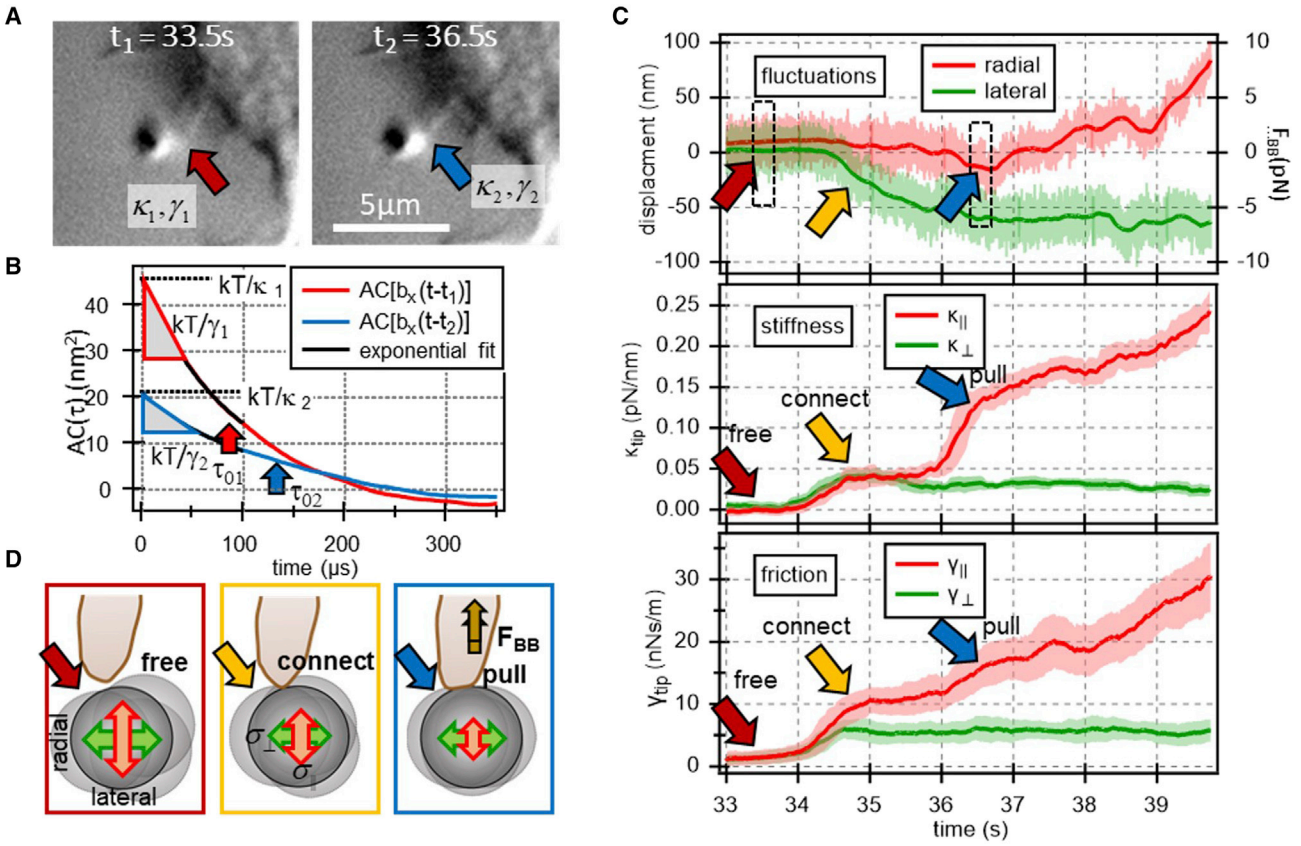

FIGURE 3 Development of binding strength and friction during filopodium binding. (*A*) Differential interference contrast microscopy images of the cell and the bead (*red and blue arrows*). The filopodium is visible, but the exact time point and strength of attachment is not visible. (*B*) The connection parameters κ and γ (at time points t_1 and t_2) are extracted from the autocorrelation function AC(τ) of the bead trajectory that changes upon binding. (*C*) Mean displacements (*dark colors*) and position fluctuations (*light colors*) of the bead, binding stiffness κ_{tip}, and friction γ_{tip}. Depicted are values for κ and γ in directions radial ($\parallel$, *red*) and lateral ($\perp$, *green*) to the filopodium. The three arrows indicate the different stages of binding. (*D*) Sketch of the fluctuations of the bead during the three stages of binding indicated by the colored arrows: dark red: before contact; orange, initial bead attachment; blue: strengthening of the bond during pulling. To see this figure in color, go online.

Bead fluctuations reveal binding stiffnesses: The model

On short timescales $t << t_L \approx 5$ ms, bead transport is negligible, i.e., $v_{BB} \approx 0$ (see Eq. 1). The bead performs a diffusive overdamped motion driven by thermal forces $F_{th}(t)$, resulting in a particle trajectory $\mathbf{b}(t) = (b_x(t), b_y(t), b_z(t))$, which gives access to important molecular parameters. In this case, Eq. 1 reads $(\gamma_{bd} + \gamma_{tip})\dot{b}(t) + (\kappa_{opt} + \kappa_{tip})b(t) = F_{th}(t)$, which corresponds to diffusive motion in a single 3D harmonic potential.

Approximating quasi-thermal equilibrium, the equipartition theorem $\frac{1}{2}\kappa_{tot}(t_L)\cdot\sigma(t_L)^2 = \frac{1}{2}k_BT$ provides reliable values of the total stiffness $\kappa_{tot} = \kappa_{opt} + \kappa_{tip}$ for each time point t_L by measuring the root-mean-square fluctuation widths $\sigma = \sqrt{\langle b(t)^2 \rangle}$ within time windows of about 5 ms, corresponding to 5000 points. By fitting the exponentially decaying autocorrelation function $AC[b_j(t)] = \langle b_j(t)^2 \rangle \exp(-\tau/\tau_{0j})$, the autocorrelation times $\tau_{0j} = \gamma_j/\kappa_j$ in lateral and radial direction $j = \perp, \parallel$ (Fig. 3 *D*) and the total viscous drag on the bead $\gamma_{tot,j} = \gamma_{bd,j} + \gamma_{tip,j}$ are also obtained according to

$$AC(\tau, t_L) = \frac{k_BT}{\kappa_j(t_L)} \cdot \exp\left(-\tau \cdot \frac{\kappa_{tot,j}(t_L)}{\gamma_{tot,j}(t_L)}\right). \quad (3)$$

The resulting mechanical parameters $\kappa_{tip,j}(t_L) = \kappa_{tot,j}(t_L) - \kappa_{opt,j}$ and $\gamma_{tip,j}(t_L) = \gamma_{tot,j}(t_L) - \gamma_{bd,j}$, obtained for each time window, are plotted over the course of an experiment in Fig. 3 *B*.

Bond strength at filopodia tips increases with pulling force

We observed that the measured bond stiffness κ_{tip} and the measured friction parameter γ_{tip} at the filopodia tips in direction of the pulling force F_{BB} (radial direction) are not constant but evolve dynamically during retractions for different bead trajectories $r_{\parallel}(t)$ or retraction forces $F_{BB}(t)$,

as depicted in Fig. 4 *A* and *B* (and Fig. S5). Although stiffness and friction values vary between experiments and over time, depending on the architecture, thickness, and length of filopodia, we found that, in general, both bond stiffness $\kappa_{tip}(F_{BB})$ and friction $\gamma_{tip}(F_{BB})$ increase under load F_{BB}. In the investigated force range between 0 and 30 pN, the average bond stiffness increases threefold and the average friction twofold (Fig. 4 *B*) A very similar result is provided by our computer simulations, as discussed later.

Based on this increase in stiffness of the bead tip connection, the simplest assumption is that the number $N(t, F_{BB})$ of bonds attached at filopodia tips increases. These bonds form the mechanical link between the bead and the stiff actin core, as sketched in Fig. 4 *C*. The attached adhesion molecules at filopodia tips form a bond cluster, and the applied load is distributed among the bonds. Mechanically, each molecular adhesion protein can be seen as a Kelvin-Voigt element that is defined by its physical properties, which are the protein elasticity, defined by the bond stiffness κ_{bnd} and the protein viscous properties, i.e., the friction parameter γ_{bnd} (see Eq. 4). As bonds at the tip are mechanically arranged in parallel, their individual properties are summed up as indicated in Fig. 4 *C*. A rise in the overall bond stiffness κ_{cell} therefore points to an increase of individual binding proteins, which increases the stiffness of the overall bond. The growth of a cluster of adhesion bonds under force is, at first glance, counterintuitive. However, this force-dependent increase in stiffness has been observed in several adhesion processes, and the responsible adhesion proteins are termed catch (slip) bonds (see Fig. 5 and discussion).

Stiffness and friction of tip connection: The model

The connection between the filopodium tip and the bead is expected to be established by several bonds, which are modeled (in the simplest and most typical case) by damped molecular springs with κ_{bnd} and γ_{bnd} and which are acting in parallel to the membrane with viscoelastic parameters $\kappa_{mem}(t)$ and $\gamma_{mem}(t)$. As shown in Figs. 4 *C* and 5 *B*, the number $N(t, F_{BB})$ of bonds, which are arranged in lateral direction $j = \perp$ (bond arrangement function $A_\perp \neq A_\parallel$), varies with time and pulling force F_{BB}, such that the stiffness of the bonds can be modeled as

$$\kappa_{tip,j}(F_{BB}) \approx A_j \cdot N(F_{BB}) \cdot \kappa_{bnd} + \kappa_{mem} \tag{4}$$

and $\gamma_{tip,j}(F_{BB})$, correspondingly. Eq. 4 describes an increasing connection stiffness (friction, correspondingly) with pulling force, as shown by the dashed light blue lines in Fig. 4 *B* (i.e., for the case $N(F_{BB}) \sim F_{BB}$).

Catch-bond cluster model of filopodia tips

As further analyzed in Fig. 6, the bead-filopodium connection reveals a sawtooth-like bead retraction trajectory and

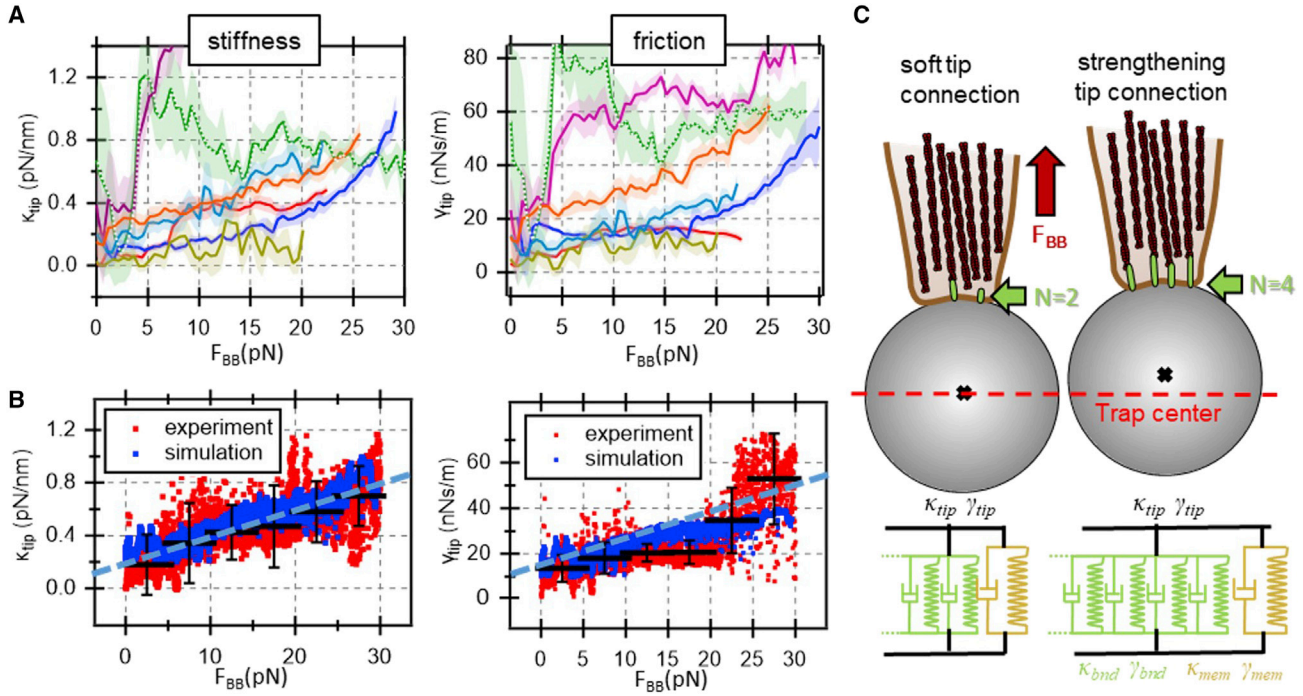

FIGURE 4 Characteristics of bonds at filopodia tips. (*A*) Dependence of the radial stiffness κ_{tip} and radial friction γ_{tip} of the bond under load F_{BB}. Different colors show the parameters from seven independent retraction experiments. (*B*) The red dots show averaged values from the seven experiments depicted in (*A*). Vertical and horizontal black error bars are STDs. In direction of retraction, the radial bond stiffness and bead damping increase under load. Blue dots are the results from the simulation. The dashed light blue line represents the analytical model. (*C*) Sketch for bond formation at filopodia tips, where more bonds connect under force. Mechanical properties of individual bonds add up, leading to increased stiffness and friction. To see this figure in color, go online.

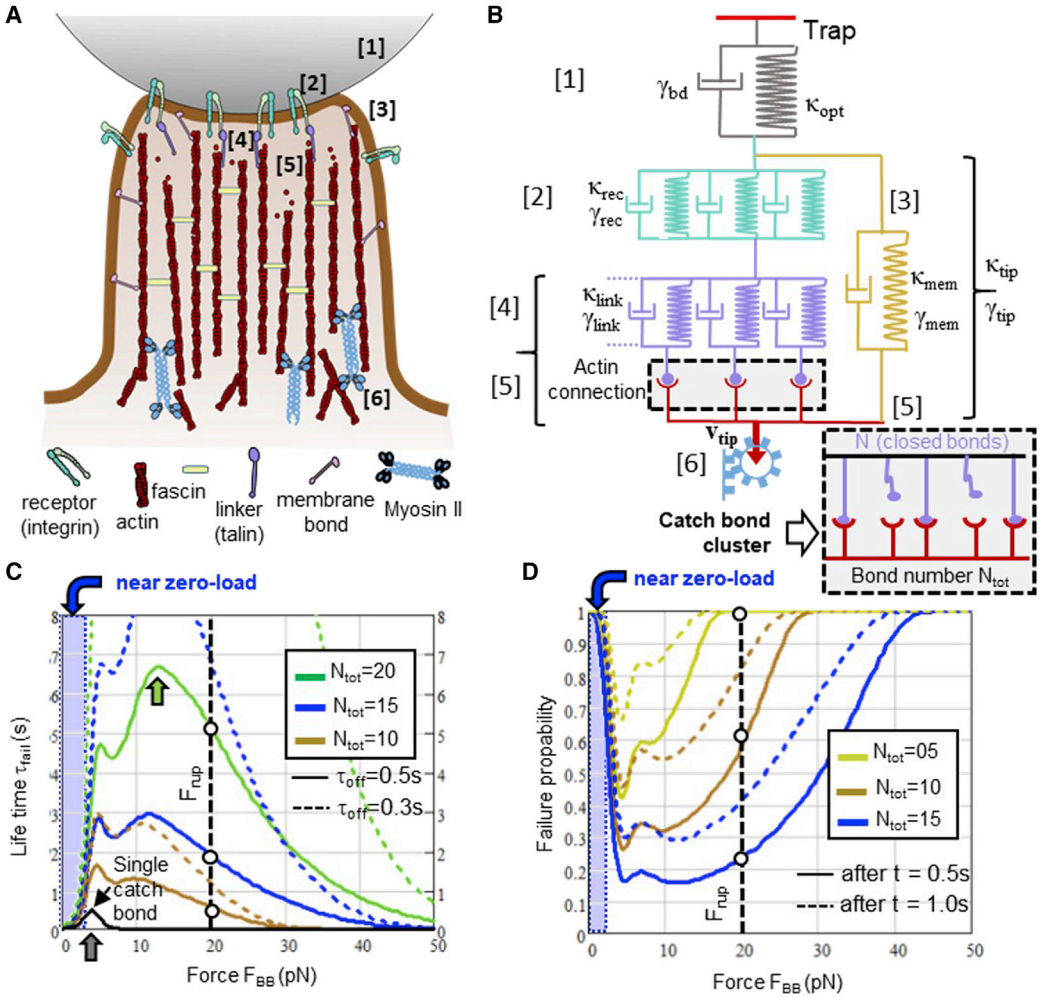

FIGURE 5 Model of filopodia architecture and molecular mechanics. (*A*) Mechanistic model for force transduction with relevant proteins. The integrin-talin protein complex used to illustrate this model fits with our observations. (*B*) Corresponding mechanical model as basis for the mathematical description. The temporal increase of $\kappa_{tip}(t)$ and $\gamma_{tip}(t)$ and especially the actin linker connection are important to explain the observations. Catch-bond clusters with force-dependent lifetimes $\tau_{fail}(F)$ describe the dynamics of the attachment of N_{tot} linker proteins, from which $N(t)$ bonds maintain the connection to the actin BB (*dashed box*). (*C*) The maximum lifetime $\tau_{off} = 0.5$ s at $F_{max} = 4$ pN of a single catch bond increases to, e.g., 6.5 s at $F_{max} = 13$ pN (see *gray and green arrows*) for a cluster of $N_{tot} = 20$ bonds. For $\tau_{off} = 0.3$ s, the lifetimes increase strongly (*dashed lines*). The vertical black dashed line marks lifetimes $\tau_{fail}(N_{tot})$ at a typical rupture force of $F_{rup} = 20$ pN. (*D*) Corresponding failure probability changing with pulling force for three different cluster sizes N_{tot} and two different pulling times. At near-zero loading force, the failure probability approaches 100%, thereby inhibiting bead retraction. To see this figure in color, go online.

quickly changing viscoelastic properties. How can this observation be explained by several molecular key players enabling force transduction in the filopodium tip? As illustrated in Fig. 5 *A*, we model changes in viscoelasticity and ruptures with a minimal mechanistic picture, which results in the mechanical (mathematical) model based on Kelvin-Voigt elements (i.e., damped springs) sketched in Fig. 5 *B*. As explained later, the connection between the optically trapped bead (in gray, κ_{opt} and γ_{bd}) and tip must be arranged in series. For our mechanistic (Fig. 5 *A*) and mathematical (Fig. 5 *B*) model, we assume that several parallel receptors (green) are connected in series to several parallel linkers (purple). This connection shows a catch-slip-bond on-/off-binding behavior to actin (red) depending on the loading force F_{BB} of the actin BB, which is generated by myosin II motors (blue) (see also Eq. 5). For a rupture of all N bonds after the time τ_{fail} leading to a failure in filopodia pulling, it is the serial connection between membrane and bead (brown/rose) that prevents the bead relaxation to the trap center ($F_{opt} = 0$). If the membrane detaches from the tip of the filopodium, as seen during failure events, a short membrane tube (<100 nm length) is pulled out at the tip.

Number of catch bonds at tip: The model

The number of closed bonds $N(t,f)$ depends on the momentary pulling force $f = F/N$, which is assumed to be equally distributed over the N bonds. The rate equation can be

approximated by $\dot{N} = k_{on}\cdot(N_{tot} - N) - k_{off}\left(\frac{1}{N}F\right)\cdot N = v(N,k_{on}) - u(N,F)$, with rebinding rate $v(N)$ and unbinding rate $u(N,F)$. Here, N_{tot} is the total number of available bonds and k_{on} the constant on-binding rate, whereas the force off-binding-dependent rate is $k_{off}(F) \approx k_0\cdot\exp(-(F+F_c)/F_0)+k_0\cdot\exp((F+F_s)/F_0)$ (25,26). The term $k_{off}(F)$ is a catch-slip off-binding rate, which decreases for moderate forces and increases for stronger pulling forces. This behavior is typical for catch (slip) bonds such as integrins (see also catch-bond cluster model of filopodia tips and section S8 in the supporting material). Here, $F_0 = kT/\delta$ is a characteristic force corresponding to the (s)lip-(c)atch path length δ (kT = thermal energy). The zero force is rate $k_{off}(0) \approx k_0\cdot\exp(-F_c/F_0) + k_0\cdot\exp(F_s/F_0)$. At the force $F_{max} = ½\,(F_s + F_c)$, a single catch bond has a maximum lifetime $\tau_{off}(F) = 1/k_{off}(F)$ (Fig. 5 *C*, *black curve*). For a talin-actin bond, we estimated $\tau_{off} \approx 0.5$ s at $F_{max} \approx 4$ pN (24).

For the steady-state $\dot{N} = 0$ or $v(N) = u(N,F)$, the relation between closed bonds N and pulling force $F(N)$ up to a maximum rupture force F_{rup} can be determined (see section S9 in the supporting material).

The lifetime of the bond cluster $\tau_{fail}(N_{tot},F)$ can be obtained by summing up the unbinding rates $u(N,F)$ of the number $N_s \approx N_{tot}/2$ of bonds in equilibrium, weighted by the ratios of re- and un-binding rates, $v/u = k_{on}(N_{tot} - N)/k_{off}\left(\frac{1}{N}F\right)N$, of each bond (26,27).

$$\tau_{fail}\left(N_{tot},F\right) = \sum_{n=1}^{N_s}\left(\frac{1}{u(n,F)} + \sum_{m=n+1}^{N_{tot}}\left(\frac{1}{u(n,F)}\prod_{i=n}^{m-1}\frac{v(i,k_{on})}{u(i,F)}\right)\right) \quad (5)$$

This average time $\tau_{fail}(N_{tot},F)$ between failures of the cluster (see Figs. 6 *B*, 7 *A*, and S11) first grows and then shrinks with the BB pulling force F as shown in Fig. 5 *C*. Here, one can see that the maximum lifetime increases with pulling force and that the overall lifetime increases with the total number N_{tot} of bonds involved. For small catch-bond clusters with $N_{tot} \leq 15$ and $\tau_{off} = 0.5$ s, one obtains lifetimes $\tau_{fail} = 0.1$–3 s close to the experimental values. However, for slightly shorter single-bond lifetimes (e.g., $\tau_{off} = 0.3$ s; Fig. 5 *C*, *dashed lines*) or slightly higher bond number ($N_{tot} = 20$) lifetimes quickly become much larger than the measured lifetimes.

The failure probability $p_{fail}(t,N_{tot},F) = 1 - \exp(-t/\tau_{fail}(N_{tot},F))$ increases monotonically with time and reaches the 100% value the earlier, the lower N_{tot}. However, the rupture probability as a function of pulling force decreases strongly until the maximum single-bond force $F_{max} = 4$ pN is reached (Fig. 5 *D*). For $F > F_{max}$, the probability increases again but rather differently depending on N_{tot} and the pulling time. For example, after t = 1 s of pulling at $F = 15$ pN with $k_{on} = 2$ Hz, one finds for $N_{tot} = 5$ and $N_{tot} = 15$, $p_{fail}(1s,5) = 92\%$ but $p_{fail}(1s,15) = 17\%$ or at $F = 5$ pN, $p_{fail}(1s,5) = 46\%$ but $p_{fail}(1s,\ 15) = 16\%$. See also Fig. S12.

Bead retractions are interrupted by failures and reconnections

When macrophage filopodia retract optically trapped beads, they can exert significant forces in order to pull the bead out of the optical trap (stronger than forces exerted by HeLa cells (8)). Any loading force is transmitted via the receptors attached to the bead and is ultimately transferred to intermediate proteins linking bead and actin BB and molecular motors pulling at the cortical BB end.

In our experiments, we have regularly observed in several (but not all) retractions that the pulling of the bead is interrupted by sudden failure events (33 failures in total). These events, shown exemplarily in the trace of Fig. 6 *A* by orange arrows, are characterized by sudden snap backs of the bead toward the trap center. Within the fraction of a second (the time τ_{poly}), the bead drifts in a rearward direction over some 10 nm (the distance x_{gap}) before the transport restarts at velocity $v_{BB}\cdot Q_T$ (see Fig. 6 *B* and Eq. 2). The time between two ruptures is the lifetime of the bond cluster τ_{fail}. For small forces ($F_{BB} < 5$ pN), we find $\tau_{fail} = 28$s on average, which drops off to 2–4 s for forces in the range 5–30 pN and to $\tau_{fail} = 0.5$ s for $F_{BB} > 30$ pN (see Fig. 6 and section S5 in the supporting material).

Pulling, failing, and reconnection between bead and actin BB are illustrated in the sketch of Fig. 6 *C*. The repetitive, sawtooth-like trajectories are characterized by a maximum in the BB pulling force F_{rup} (rupture force) or by the bead displacement x_{rup} and a decay to a new minimal holding force termed F_{mem}, for reasons explained later, corresponding to a bead position x_{mem} (Fig. 6 *B*).

Analysis of the fluctuation data (Fig. 6 *A* and *B*) reveals that the filopodium does not disconnect completely during these failure events, since the bead does not snap back to the trap center but rather stops at a position x_{hold}. Correspondingly, the measured counteracting force relaxes to a minimum $F_{mem} = \kappa_{opt}\cdot x_{hold}$, which characterizes the remaining soft connection to the bead. In addition, both radial stiffness and friction decay/increase from values $(\kappa_{rup},\gamma_{rup})$ to $(\kappa_{mem},\gamma_{mem})$ are roughly proportional to the BB pulling force (Fig. 6 *D*) and are still significantly larger than those of a purely optically trapped bead $(\kappa_{opt},\gamma_{bd})$. Hence, the filopodium tip is still attached to the bead and must stretch during the snap back of the bead without detaching. As further proof of this hypothesis, we found BB rupture relaxation times $\tau_{rup} \approx 4$ ms by exponential fitting, which are significantly longer than relaxation times of optically trapped beads in solution. The fluctuation data taken

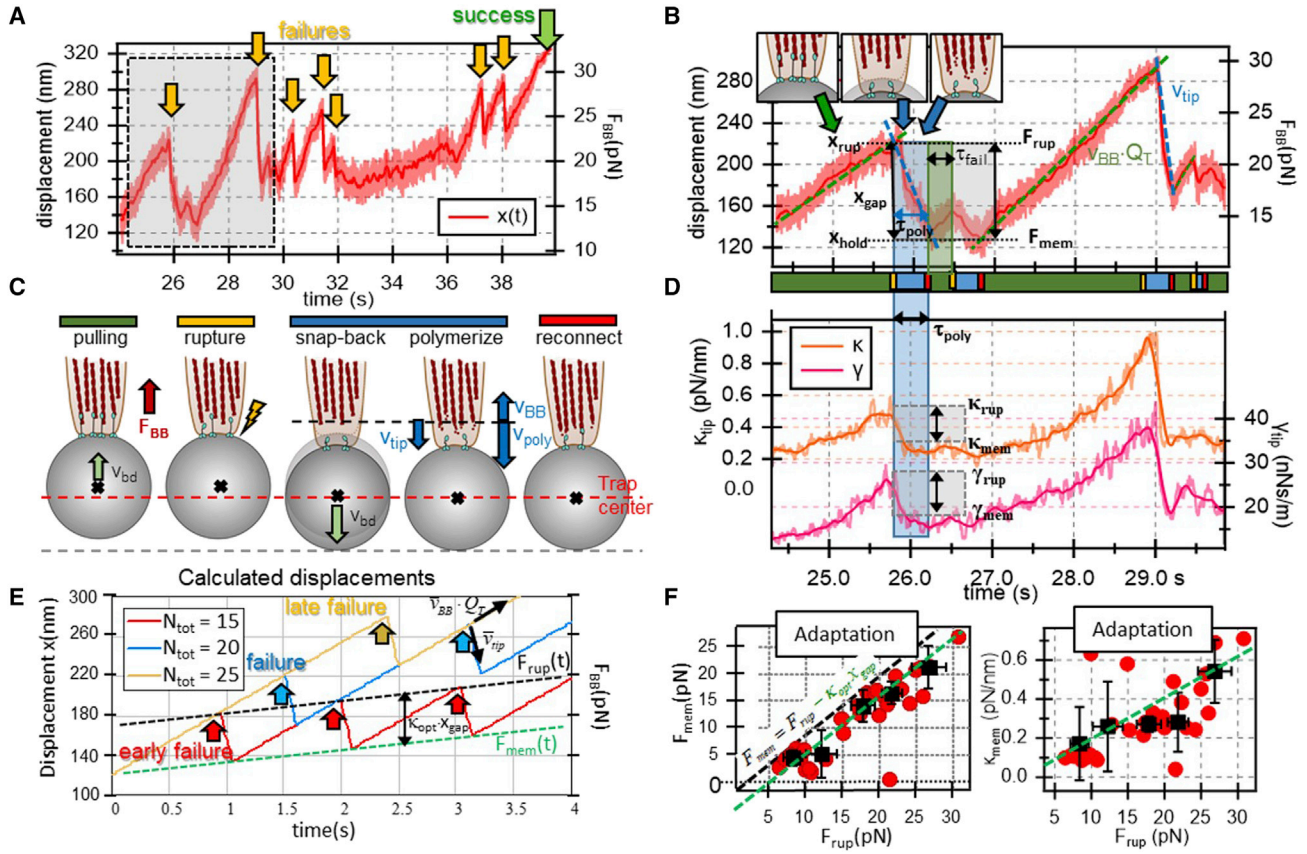

FIGURE 6 Failure events during retractions. (*A*) After multiple failures during one retraction, the filopodium succeeds and pulls the bead out of the trap. (*B*) Five second time window showing the sawtooth-like characteristics in time and space of the trajectory with intermittent failure events. Forward motion is indicated by green and backward motion by blue dashed lines. Fluctuation parameters κ_{tip} and γ_{tip} of the tip connection decrease and increase correspondingly (*D*). (*C*) Sketch illustrating the velocities and forces occurring in the figures above during failure and reconnection. (*E*) Calculated bead displacements and failures during retraction for different bond numbers N_{tot}. Early (*red*) and late (*orange*) failures until rupture (see *arrows*) change with N_{tot}. The minimal holding force F_{mem} (*green dashed line*) increases parallel to the rupture force F_{rup} (*black dashed line*) over time. The force difference is the loading force $\kappa_{opt} \cdot x_{gap}$. (*F*) Measured force adaptation: the membrane holding force and stiffness κ_{mem} (*green dashedlines*) increases parallel to the rupture force (*black dashed line*), analyzed from 30 rupture events from 7 independent pulling experiments. The force difference is $dF \approx 4$ pN $= \kappa_{opt} \cdot 40$ nm. Shown are raw data points (*red*) and the pooled data points (*black*). Vertical and horizontal black error bars are STDs. To see this figure in color, go online.

together point to a sequence of events that occur during failures as shown in Fig. 6 *C* and that will be detailed in the discussion. The calculation results shown in Fig. 6 *E* should reproduce the experimental results of Fig. 6 *B* and *D* to test our understanding. This minimal analytical model is based on the bead velocities in forward ($v_{BB} \cdot Q_T$) and backward (v_{tip}) directions, on a fixed polymerization time τ_{poly}, and on a force-dependent time to the next failure $\tau_{fail}(F)$ based on Eq. 5. From these four parameters, the model produces a rupture force F_{rup} and a minimal holding force F_{mem}, which both can increase over time. This is explained by the following "rupture and reconnection" model.

Fig. 6 *F* demonstrates that both the minimal holding force F_{mem} and stiffness κ_{mem} increase after failures with the rupture force F_{rup}, which is necessary to induce the failure. In total, 30 BB rupture events are analyzed from seven retraction trajectories. The approximately linear dependency of F_{mem} and κ_{mem} on F_{rup} is explained by Eqs. 6 and 8. In the discussion, we reconsider why this is termed "adaptation."

Rupture and reconnection: The model

After all bonds have opened under load, i.e., after the mean (on) time $\tau_{fail}(F_{BB})$ according to Eq. 5, the BB ruptures from both the filopodia tip and the bead, which is still connected to the membrane, and then relaxes toward the trap center at an intermediate position x_{hold} (Fig. 6 *A* and *B*, *red trajectory*). After such a failure, it takes the (off) time τ_{poly} until bead transport continues with $\overline{v}_{bd}(F) = \overline{v}_{BB} \cdot Q_T(F)$ according to Eq. 2. The time $\tau_{poly} = x_{gap}/\overline{v}_{tip}$ is the time the BB (elongating at velocity $\overline{v}_{tip}$) needs to close the gap of length x_{gap} to the membrane by actin polymerization. The velocity $\overline{v}_{tip} = \overline{v}_{poly} - \overline{v}_{BB}$ is the polymerization speed $\overline{v}_{poly}$ reduced by the constant retrograde flow velocity $\overline{v}_{BB}$ of the BB. As displayed in

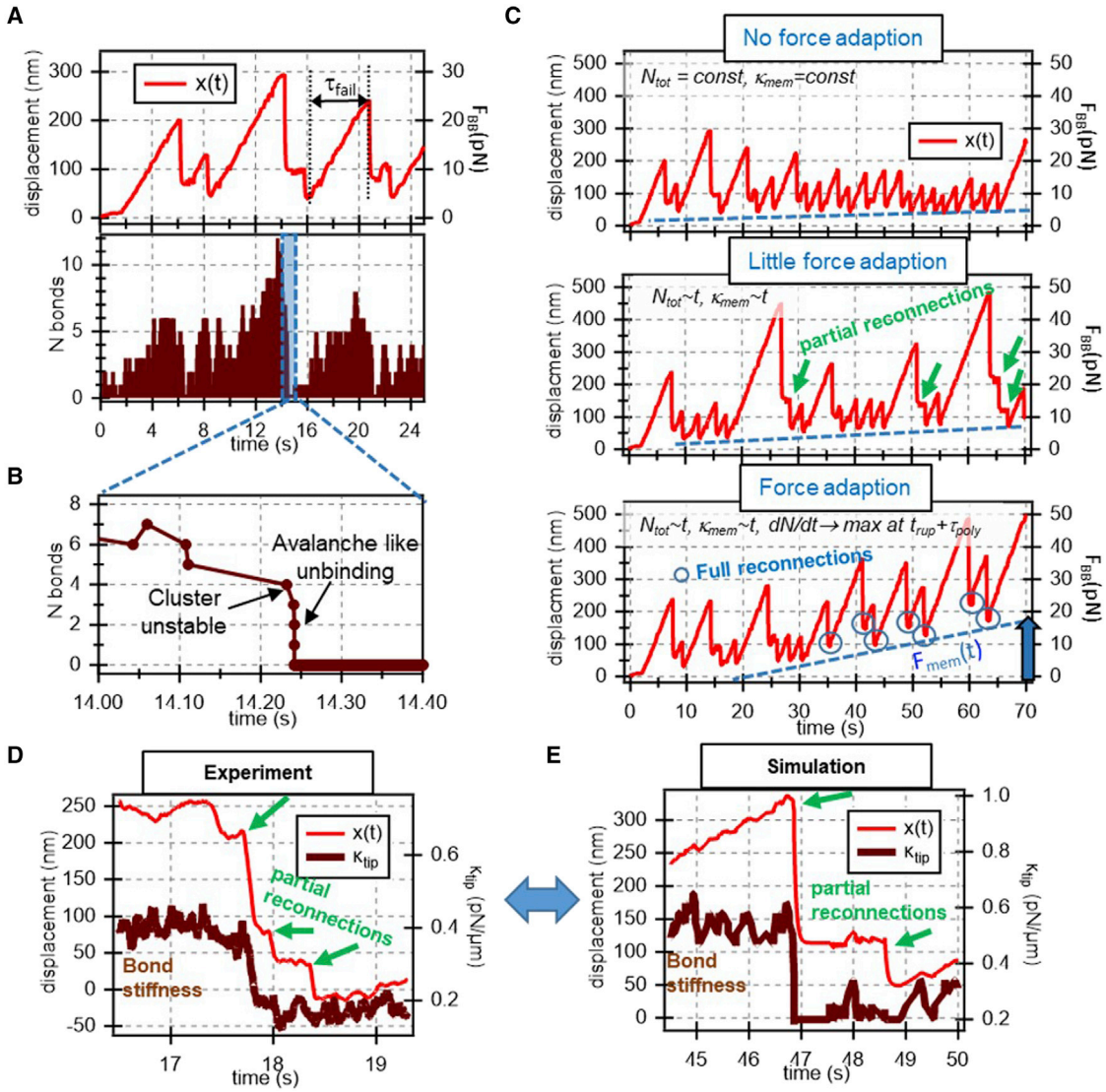

FIGURE 7 Results of simulations of filopodia retractions. (*A*) Simulated trajectory for bead displacement and force (*red*) and corresponding bond cluster dynamics (*dark brown*). Although the number of bound bonds N(t) varies during pulling, the average of N(t) increases linearly until failure occurs. (*B*) Failure event within a 400 ms time window: as the number N of bound bonds drops below a critical value, remaining bonds unbind avalanche-like until N = 0. (*C*) Without load-dependent adaptation of the filopodium, the retraction curve does not rise (*top*). Considering a steady increase of $\kappa_{rup}(t) = \kappa_{mem}(t) + N_{tot}(t) \cdot \kappa_{bnd}$ with N_{tot} bonds and stiffness κ_{mem}, the forces F_{rup} until rupture increase, but partial reconnections (*green arrows*) prevent an increase in holding force F_{mem} (*middle*). For a catch-bond cluster rebinding at once (force independently) after ruptures, partial reconnections become rare, leading to a characteristic increase in F_{mem} (*bottom*) by a series of full reconnections (*blue circles*). (*D*) Partial reconnection events (*green arrows*) as seen frequently in measured trajectories. (*E*) Observed partial reconnections in simulations with comparable characteristics as in (*D*). To see this figure in color, go online.

Fig. 6 *B*, *C*, and *E*, a failure occurs at rupture time t_r and displacement $x_{rup}(t_r)$ with force $F_{rup}(t_r) = \kappa_{opt} \cdot x_{rup}(t_r)$ and with bead fluctuations resulting in $\kappa_{rup}(t_r)$ and $\gamma_{rup}(t_r)$. After the gap filling time τ_{poly} and distance $x_{gap} = x_{rup} - x_{hold}$, the bead relaxation comes to an end at time $t_s = t_r + \tau_{poly}$ and displacement $x_{hold}(t_s)$. This corresponds to a hold force $F_{mem}(t_s)$, which is just the membrane force that slows down the snap back of the bead into the trap center. We find $F_{mem}(t_s) = \kappa_{opt} \cdot x_{hold}(t_s) = \kappa_{opt} \cdot (x_{rup}(t_r) - x_{gap}(t_s))$, and hence

$$\begin{aligned} F_{mem}(t_s) &= F_{rup}(t_r) - \left(\kappa_{opt} \cdot x_{gap}(t_s)\right) \\ &= F_{rup}(t_r) - \left(\kappa_{opt} \cdot v_{tip} \cdot \tau_{poly}\right). \end{aligned} \tag{6}$$

Fig. 6 *E* illustrates this relation by a calculated, sawtooth-like bead retraction trajectory over 4 s including pulling and failure (see calculated x(t) in sections S12 and S13 in the supporting material). The time until failure (see $\tau_{fail}(F)$ in the next section) increases with the number of bonds N_{tot} and so does the membrane force $F_{mem}(t_s)$. The experimental

results of Fig. 6 *F* confirm the relationship in Eq. 6. In particular, they show a force adaptation in the sense that the membrane force $F_{mem}(t_s)$ increases with the rupture force $F_{rup}(t_r)$. The latter is always slightly larger by the small mean force difference $\kappa_{opt} \cdot \langle x_{gap}(t_s) \rangle \approx 100 \frac{pN}{\mu m} \cdot 50nm = 5$ pN, as indicated by the black and blue dashed line.

After all bonds have opened within $\tau_{fail}(F)$, the number of closed bonds $N(t, F)$ drops to zero, and the connection stiffness and friction drop to $\kappa_{mem}(t_s)$ and $\gamma_{mem}(t_s)$. Based on the assumptions in the equations above, the change in stiffness can be described by

$$\kappa_{rup}(t_r, F) = \kappa_{mem}(t_s, F) + N(t_r, F) \cdot \kappa_{bnd} \tag{7}$$

and $\gamma_{rup}(t_r)$ correspondingly, which agrees with the experimental result of Fig. 6 *D*. Solving for κ_{mem} and replacing κ_{mem} with the optical force per rupture length, one can see that the minimum stiffness of the rupture, i.e., the connection of the bead to the membrane can be written as

$$\kappa_{mem}\left(F_{rup}\right) = F_{rup} \cdot \frac{1}{x_{rup}} - N(t_r, F) \cdot \kappa_{bnd}, \tag{8}$$

in agreement with the results of Fig. 6 *F*, where $\kappa_{mem} \approx 100 \ldots 600$ pN/μm increases approximately linearly with F_{rup}.

Numerical catch-bond cluster simulation reproduces failures and adaptation

In addition to the simplified analytical model and based on the equations, we performed numerical computer simulations, which gave us the possibility to compare the bead displacement $x(t)$ relative to the loading force $F_{BB}(t)$ and the number $N(t)$ of bound linkers between the bead and the actin BB. In addition, the model should give answers about the mechanisms and times for reconnections between BB and membrane, which is elementary for efficient filopodia pulling. The situation at filopodia tips was modeled as a cluster of catch bonds with stochastic binding and force-dependent stochastic off binding using a Gillespie algorithm (28). The rearward pull of the actin BB was simplified as a backward motion with constant velocity v_{BB}. The parameters used to describe the mechanical protein properties are partly derived from measurements but are also based on meaningful assumptions, which can be found in Table S1.

The results shown in Fig. 7 are arranged in a comparable style to the experimental results in the previous figures. Fig. 7 *A* displays a simulated trajectory for a bead displacement and the proportional pulling force (red), together with the corresponding bond cluster dynamics (dark brown). Here, the number of closed bonds $N(t)$ fluctuates considerably during pulling, whereas the average of $N(t)$ increases approximately linearly under force. When forces become too high, the cluster collapses, leading to a failure event. Fig. 7 *B* displays a zoom in on one failure event: as the number of bound bonds N drops below a critical value, the remaining bonds unbind in an avalanche-like manner until $N = 0$. Fig. 7 *C* shows that the lifetime of the catch-bond cluster depends nonlinearly on the loading forces and the number of bonds (29). Without load-dependent adaptation of the filopodium tip connection, the retraction curve does not rise (first graph), and a force threshold is visible. Assuming a continuous increase of bonds $N_{tot} \sim t$ and total stiffness $\kappa_{mem} \sim t$ with time, as shown in the graph, filopodia pulling against higher forces becomes possible, and rupture forces increase. However, sequential failures (green arrows), i.e., incomplete, partial reconnections prevent a significant increase in displacement and holding force F_{mem} over time (second graph). Remarkably, partial reconnections are rare for a simulated catch-bond cluster, which rebinds constantly, i.e., independent of force after ruptures, leading to a characteristic increase in F_{mem} over time (third graph). This increase in the minimal (holding) force (blue dashed line) is what we call adaptation.

Partial reconnections (green arrows) occur in simulated trajectories, as depicted in Fig. 7 *E*, when the catch-bond cluster cannot rebuild in time under load. Partial reconnections with very similar characteristics can be observed also in some experiments (Fig. 7 *D*) but can be recognized only rarely.

DISCUSSION

How can one image and understand processes that are invisible with common microscopy technology? Fig. 1 shows high-quality fluorescence and bright-field images of filopodia connecting to an optially trapped bead but without making the connection visible. Through its actin BB, the filopodium repetitively pulls at the bead and fails until—in some cases—it succeeds and withdraws the bead. In most cases, however, the pulling force transduced by the filopodium tip increases with subsequent failures. This is what we call adaptive mechanotransduction. The filopodium connection to the trapped bead is invisible, but it changes continuously in strength, structure, and dynamics during filopodia pulling. We revealed these changes in connection by the fluctuation displacements of the bead, which we measured interferometrically in 3D at microsecond resolution and with nano-meter precision. To better understand our results, we have established a mechanistic model (as summarized in Fig. 5) based on bead motions, where the actin BB inside the filopodium is viscoelastically connected by molecular linkers to the cell membrane and then to the bead (outlined in Fig. 1 *C*). This mechanistic model is substantiated and confirmed by the results from an analytical mathematical model and from numerical computer simulations, where we minimized the number of components and parameters.

Mathematical modeling

The number of biophysical components defined the number of parameters in our models, which becomes apparent by 1) looking at the multiple-bond tip connection and 2) a description of the sawtooth-like bead displacements. The latter is characterized by times of polymerization or times until failure by the length x_{gap}, the BB velocity or the tip velocity (slopes of the sawtooth curves), and the corresponding rupture force and the minimal holding force (identified as membrane force). Most of these parameters have been taken from the experiments. The missing parameters, e.g., for the catch-bond model, have been taken from the available data from literature by testing the influence of unknown parameter variation for the analytical model (see section S16 in the supporting material). The influence of the catch-bond cluster dynamics was also investigated by performing stochastic simulations (see text of Fig. 7).

Hence, it is not important whether the number of available bonds is $N_{tot} = 10$ or 20 or whether the forces are 10 or 20 pN (which are all values occurring in our experiments), but it is important to learn that they are within the correct order of magnitude and how they influence the slope of the rupture curve. This way the model helps to understand and confirm our mechanistic model.

Our mechanistic model allows us to explain several observations during filopodia pulling, among which a very striking effect is failing and rupture on the one hand but an increase of the tip connection strength and the pulling force on the other hand. This adaptation of the cellular retraction system allows the immune cell to increase its efficiency during capture and uptake of particles and pathogens.

Bead transport slows down under load, but retrograde flow remains constant

Using oblique, confined fluorescence illumination, we could significantly increase the image contrast of a single dorsal filopodium. Thereby, we were able to observe that the velocity of actin EGFP speckles (the retrograde flow velocity) equals the bead retraction velocity when there is no loading force. However, under load of 5 … 30 pN (exerted by the optical trap), the bead transport is, on average, about three times slower than the actin backward flow driven by myosin motors in the cortex (see Fig. 2). This indicates a continuous on and off binding at the tip, such that bead transport—although on nonmeasurable timescales—is interrupted more often than it is established (duty ratio $Q_T(F>0) = \frac{\overline{v}_{bd}(F)}{\overline{v}_{BB}} = \frac{\tau_{on}(F)}{\tau_{on}(F)+\tau_{off}} \approx 1 \div 3$). From $Q_T = 1 \div 3$ we find that bead and membrane bind to actin with the averaged on- and off-binding times $\tau_{off} = 2 \cdot \tau_{on}(F>0)$, a behavior typically for molecular clutchs known from the integrin-talin complex. Since no measurable stops are visible during regular bead transport, the actin polymerization at the BB seems to close any gaps quickly (we found $\tau_{off} = \tau_{poly} = x_{gap}/v_{tip} \approx 0.1$s) and on short distances below the optical resolution limit. Within τ_{off}, the polymerization velocity must be much faster than the BB retrograde flow, which was found to be $v_{BB} = 0.17 \pm 0.07$ μm/s. Remarkably, actin retrograde flow does not decrease under force, and stands in contrast to previous assumptions that retrograde transport is limited by the ability of motor proteins to pull against force (5).

We want to point out that the mathematical model fits well to the following two experimental observations (Fig. 2 *G*): i) a threefold decrease in transport velocity for loading forces $F > 4$ pN, and ii) high bead transport velocities v_{bd} (nearly 90% of the BB velocity) at low loading forces $F < 4$ pN. This combination was only possible with low bond numbers ($N_{tot} = 5$–15) together with short off-binding times $\tau_{off} = \leq$ 0.1 s–0.5 s. For future experiments it would be challenging to confirm and estimate N_{tot} by fluorescence stoichiometry, the off-/on-binding times by high-resolution fluorescence tracking of f-actin end proteins.

Connection strength at tip increases with number of bonds during filopodia retraction

Using fast photonic force microscopy measurement technology with MHz bandwidth, we read out increases in bond stiffness and viscosity with increasing pulling force F_{BB} through nm changes in fluctuation widths and microsecond changes in position correlations. We attribute the observation depicted in Fig. 4 to an increase in the overall number of engaged bonds. We minimized measurement artifacts after careful corrections for calibrations of nonlinearities (see sections S2 and S3 in the supporting material). Bead fluctuations decrease in amplitude and relaxation time upon contact and during bead retraction (Fig. 3 *C* and *D*), which is equivalent to an increase in binding strength and friction during retraction (Fig. 3 *A*). This behavior is typical for enthalpic springs and cannot be explained with entropic springs, which require too long to form a significantly high gradient in state density during continuous BB transport. The bond strength $\kappa_{tip}(F_{BB})$ increasing with force F_{BB} is visible only in pulling direction, whereas the lateral strength remains constant, i.e., no further lateral connections at the tip are established over time. This can be explained by the long, slender architecture of the potential key players, integrins (19) and talins, which switch between active and inactive states (20) to connect the receptor (through vinculin) to the actin fibers (20,21), each with elasticity κ_{bnd}. The changing connection strength can be explained as follows: whereas lateral (angular) fluctuations of the bead center appear amplified by the $R = 500$ nm distance of the connection point to the bead center, the radial stiffness increases over time likely because of an increasing number $N(t)$ of elastic bonds (integrin clustering), such that $\kappa_{tip}(F_{BB}) \sim N(F_{BB}) \cdot \kappa_{bnd}$ (Eq. 4). This is not in contradiction to the continuous on/off binding of the linkers mentioned above.

Catch-bond cluster regulates force transduction at filopodia tips

Various adhesion proteins are enriched at filopodia tips, and it is likely that several proteins are involved in binding (12) and that attachments are regulated by clusters of bonds. This allows the conclusion that the total number of available bonds N_{tot} increases steadily by diffusion or active myosin X transport to the tip (30), which does not mean that the number of closed bonds $N < N_{tot}$ increase in the same way. This is the case for catch (slip) bonds, which reveal a lifetime τ_{fail} first increasing at low forces up to a maximum F_{max} and only then decreasing again for higher forces ($F_{BB} > F_{max}$), similar to slip bonds (Fig. 5 *C*). The integrin-talin-actin molecular clutch illustrated in Fig. 5 is a well-known catch-bond complex, which fits with our experimental observations (29). For an F-actin-talin bond, we estimated $\tau_{\mathrm{fail}} \approx 0.5$ s at $F_{max} \approx 4$ pN in barbed end pulling direction (24). Based on the model, the cluster lifetime at the maximum force increases nonlinearly with the number of bonds ($N_{tot} = 5$–15) leading to $\tau_{fail} = 0.5$–3 s and a failure probability <50% for forces $F_{max} = 5$–35 pN (Fig. 5 *C* and *D*), which agrees well with our experimental observations. This variable bond lifetime is significant for many adhesion processes, including this one. The catch-bond behavior is characterized by its avalanche-like unbinding of all bonds in the cluster for loads $>F_{max}$. Exactly this was observed in our experiments (Figs. 2 *F*, 6 *B*, *C*, and 5 *D*) and was confirmed by the simplified mathematical model (Fig. 2 *G*) and by our numerical simulations (Fig. 7 *A*–*C* and *E*). We show in section S15 in the supporting material that the observed behavior of pulling, failing, and bond enforcement is not possible with slip bonds. We have investigated and shown for the first time that catch-bond clusters characterized filopodia target binding and pulling. This target binding characteristic is likely also important for other immune cells taking up counteracting pathogens and thereby for the function of the immune system.

Failures by breakage of actin-membrane links and quick repair during pulling

Filopodia pulling at high forces is interrupted by significant rupture events despite an increasing number of bonds forming a cluster at the filopodium tip (Fig. 6). This behavior could be understood by not only analyzing the mean bead positions but also the position fluctuations, which encode the binding strengths κ_{tip}. In combination with an analytical model, we could generate a mechanistic picture of failing events, consisting of pulling, rupture, snap back, re-polymerization, and reconnection as shown in Fig. 6 *C*: as pulling forces at F_{rup} become too high after time $\tau_{fail}(N_{tot}, F_{rup})$, the cluster of bonds at filopodia tips collapses, and the bead disconnects from the stiff actin BB. This is reflected in a sudden drop of the connection stiffness κ_{tip} and pulling force (Fig. 6 *B* and *D*). Subsequently, load is transferred onto the membrane, which stretches out by the distance x_{gap} and forms a small membrane tube at filopodia tips until the variable membrane holding force F_{mem} prevents further elongation. In the experiments, this process is revealed by two facts: first, the stiffness of the connection and the displacement of the bead do not drop to zero, indicating that the membrane of the filopodium is still connected to the bead. Furthermore, the strongly damped bead relaxations (see section S6 in the supporting material) of up to 200 nm point toward a deformable cellular connection, which cannot be established by proteins at the filopodium tip. Within a few 100 ms (time τ_{poly}), we see that the cellular retraction machinery resumes pulling quickly after failures. This fits well with the picture of tip ruptures in Fig. 6 *D*: as a gap forms at filopodia tips between actin and membrane, the polymerization velocity at the tip is increased (see section S7 in the supporting material), while retrograde flow remains constant (8,31). When the gap of length $x_{gap} = x_{rup} - x_{hold}$ has refilled within τ_{poly} and the first linkers have reconnected, the cell can resume pulling. The number of linkers reconnecting to the tip within τ_{poly} is decisive for the adaptive mechano-transduction, as discussed in the next section. From the mean displacements, we calculate the polymerization velocity $v_{poly} = v_{tip} + v_{BB} = 350$–550 nm/s, which is high compared to previously reported numbers for other cell types in the range of 50–200 nm/s (8,32). This fast re-polymerization allows the cell to overcome comparably high forces even in the case of initial breakage events. The connection between bead and receptor/membrane is able to withstand forces of more than 30 pN, which are higher than reported for, e.g., HeLa cells with $F_{max} \approx 17$ pN (8). From the sudden increase in the 3D fluctuations, i.e., the drop off in stiffness to a minimum level $\kappa_{hold} = \kappa_{mem}$, we clearly see that the connection ruptures directly at the tip of filopodia. Since the fluctuations reveal that the membrane is still attached, the weakest link in the connection is between actin and membrane, which makes talin a likely candidate with an estimated maximal lifetime τ_{fail} at approximately 4 pN, whereas integrin has a τ_{fail} at approximately 25 pN (19). In contrast to aforementioned studies about filopodia pulling, our experiments reveal quick repair mechanisms, which are essential for the success of macrophage filopodia pulling.

Adaptation of tip structure under force ensures success of filopodia pulling

In pulling experiments with multiple failures, we observe an overall bead retraction out of the trap in 95% of all cases, even if ruptures cause intermittent set-backs. Additionally, we see no force threshold above which retraction stops (8) since filopodia could withdraw trapped beads at $F_{opt} > 40$ pN (5,7). The overall increasing pulling force indicates that failures do not necessarily have a negative influence, which can result from several effects. Most

important is a fast reconnection of the bead to the BB (within time τ_{poly}), i.e., a fast closing of the gap by polymerization with velocity $v_{poly} = v_{tip} + v_{BB} = x_{gap}/\tau_{poly}$ (see sawtooth profiles in Figs. 6 and S15). We show by Fig. 2 that the retrograde flow velocity v_{BB} remains constant, independent of pulling force F_{BB}. We measured a slight increase in reconnection velocity $v_{tip} \sim v_{poly}$ with F_{BB}, whereas the gap length x_{gap} did not show unique dependency on F_{BB}, i.e., it remained constant on average (Fig. S8). It might be possible that the polymerization velocity might increase with larger gap sizes because of less steric hindrance. However, this will require further and more advanced experiments in the future. The BB tip must catch up to the bead relaxing toward the trap center as soon as possible. If the BB cannot elongate faster, the relaxation of the bead connected to the membrane must be slowed down in order to decrease the gap length x_{gap}. This is only possible if the membrane connection to the bead becomes stiffer and more viscous over time, and this effect was indeed observed, as shown in Figs. 3, 4, and 6 *D*. Remarkably, this effect could only be detected from high-frequency thermal fluctuations of the bead.

A possible explanation for the adaptive mechanotransduction, i.e., the increase of membrane viscosity and stiffness (Fig. 4), is a change in the lipid composition, which occurs upon many chemical or mechanical perturbations at any synthetic (33,34) or cell membrane (35). Besides liquid ordering, this includes recruitment of sphingomyelin, cholesterol, and lipids with saturated fatty acyl chains, as well as further adhesion molecules or proteins such as integrins (Fig. 7 *C*), which all lead to a change in lipid mobility and friction in the membrane. This ongoing membrane diffusion and reorganization process leads to an enhanced holding force F_{mem}, stiffness κ_{mem}, and friction γ_{mem} (Fig. 6 *B* and *C*), but whether it is even accelerated by repetitive ruptures of the BB linkers, i.e., by repetitive stimuli needs to be investigated in future studies. For instance, formins, which are one likely candidate involved in tip linking, could hinder force adaptation by using formins inhibitors (12). Established biochemical strategies, i.e., to knock out potential membrane proteins at the filopodium tip might be a further way to go, although a direct link between protein knockouts and a malfunction of the filopodia pulling mechanism is difficult to ensure.

However, only by the repetitive failures could we define the minimum holding (membrane) force F_{mem}, which indicates the required change in the membrane tip composition. Putting all the acquired knowledge from Figs. 1, 2, 3, 4, 5, and 6 together, we generated the numerical simulation, which produced the same temporal increase in the remaining membrane force F_{mem} (indicated by the *blue dashed line* in Fig. 7 *C*) and corresponds to an adaptive strengthening of the filopodium-bead connection, which becomes apparent through repetitive failures, triggered by mechanical force. What is the role of the catch-bond cluster behavior of the potential talin-integrin complex? At low forces ($F < 5$ pN), the cluster ruptures quickly, and repetitive small failures occur (although often not visible). For a sudden force increase, but not a slow increase, of the pulling force ($F > 5$ pN), however, the cluster becomes stable over a broad range of forces (Figs. 5 *C*, S11, and S12). Also, this principle is further refined by the numerical simulations: Fig. 7 *C* (*bottom*) shows that the most pronounced mechano-adaptation is only possible if the catch-bond cluster rebinds instantaneously after rupture and reconnection—independent of any pulling force. This stable situation prevents sequential short failures during reconnection (Fig. 7 *C*, *green arrows*), i.e., prevents the tip connection breaking immediately before a sufficiently stable cluster has been rebuilt. Only by careful fluctuation analyses could the concept of partial (incomplete) reconnections be identified (Fig. 7 *D*) and used for the simulations (Fig. 7 *E*) to thereby understand the nano-scale effects of force adaptation from a (bio-)physical point of view. The membrane force and tension seem to hold the bead and enable efficient repair mechanisms through stable cluster reconnections after bead-receptor-linker-actin breakages.

CONCLUSION

We have employed a combination of fast probe fluctuation measurements and computer simulations to identify nanometer scale processes at filopodia tips on times between microseconds and seconds. Our strategy is alternative to the various established fluorescence-based techniques, which reach their limits when fast tip connection changes result in motion blur, as shown in Fig. 1. However, retrograde transport of actin speckles allowed us to determine important parameters in this study. Only with the high-frequency fluctuations of the attached bead have we been able to make conclusions about the changing connection stiffness and viscosity at the filopodium tip. Without mathematical equations, we would not have known how to analyze the fluctuation data or how to identify and proof characteristic quantities describing failure and transport. This holds for the milliseconds scale, where bead transport was found to be three times slower than the retrograde actin BB flow, but also for the seconds scale, where rupture and reconnections reveal the fail and pull behavior. Through the precise and fast 3D interferometric particle tracking, we could extract actin polymerization velocities or gap lengths of 30–100 nm in the filopodia tips and, most importantly, the effect of incomplete ruptures or reconnections, which hinder the efficiency of filopodia pulling. These effects, tiny on both temporal and spatial scales, might have been disregarded without checking their relevance through numerical simulations. And last but not least, the concept of catch-slip bonds forming clusters at the filopodia tips were the decisive element to describe the observed behavior and to understand

the sensitive pulling of filopodia. Only by analytical models and computer simulations of multiple bonds within a cluster connecting to the bead could we validate the observed times between failures at measured loading forces. These models provided convincing results when based on the catch-(slip-) bond characteristics of a single talin-integrin connection. We cannot exclude other specific and nonspecific molecular binding, but with this specific catch-bond behavior, all measured results in this study could be confirmed quantitatively by the mathematical models, generating a mechanistic picture about filopodia pulling. Although future studies with fluorescence techniques, small-molecule inhibitors, or genetic up- or down-regulation must help to identify and confirm the relevant proteins at the distal end of filopodia, the goal to understand adaptation and optimization in nano-scale systems upon external stimuli will hardly be possible without computer models and microsecond data acquisition.

SUPPORTING MATERIAL

Supporting material can be found online at https://doi.org/10.1016/j.bpj.2022.07.028.

AUTHOR CONTRIBUTIONS

A.R. designed research; R.M. and A.R. performed research; N.G. and B.E. prepared cells; R.M. analyzed data; A.R. and R.M. wrote the paper.

ACKNOWLEDGMENTS

The authors thank Prof. Holger Kress, Dr. Felix Jünger, Dr. Felix Kohler, and Dr. Eva Rog-Zielinska for a critical reading of the manuscript and helpful comments and discussions. Thanks go to Prof. Wilfried Weber and Prof. Winfried Römer for support with cell transfection. We further acknowledge the discussions with Prof. Winfried Römer on membrane reorganizations. The work was funded by the German Research Foundation (DFG grants RO 3615/3-1 and RO 3615/3-2) and by the Excellence Initiative of the German Federal and State Governments (EXC 294 and EXC 2189). We also thank the Freiburg BIOSS Toolbox for help with the transfection of J774 cells.

DECLARATION OF INTERESTS

The authors declare no competing interests.

REFERENCES

1. Beedle, A. E. M., A. Williams, …, S. Garcia-Manyes. 2015. Mechanobiology—chemical origin of membrane mechanical resistance and force-dependent signaling. *Curr. Opin. Chem. Biol.* 29:87–93.
2. Gardel, M. L., I. C. Schneider, …, C. M. Waterman. 2010. Mechanical integration of actin and adhesion dynamics in cell migration. *Annu. Rev. Cell Dev. Biol.* 26:315–333.
3. Iskratsch, T., H. Wolfenson, and M. P. Sheetz. 2014. Appreciating force and shape — the rise of mechanotransduction in cell biology. *Nat. Rev. Mol. Cell Biol.* 15:825–833.
4. Huse, M. 2017. Mechanical forces in the immune system. *Nat. Rev. Immunol.* 17:679–690.
5. Kress, H., E. H. K. Stelzer, …, A. Rohrbach. 2007. Filopodia act as phagocytic tentacles and pull with discrete steps and a load-dependent velocity. *Proc. Natl. Acad. Sci. USA.* 104:11633–11638.
6. Vonna, L., A. Wiedemann, …, E. Sackmann. 2007. Micromechanics of filopodia mediated capture of pathogens by macrophages. *Eur. Biophys. J.* 36:145–151.
7. Kohler, F., and A. Rohrbach. 2015. Surfing along filopodia - a particle transport revealed by molecular scale fluctuation analyses. *Biophys. J.* 108:2114–2125.
8. Bornschlögl, T., S. Romero, …, P. Bassereau. 2013. Filopodial retraction force is generated by cortical actin dynamics and controlled by reversible tethering at the tip. *Proc. Natl. Acad. Sci. USA.* 110:18928–18933.
9. Mattila, P. K., and P. Lappalainen. 2008. Filopodia: molecular architecture and cellular functions. *Nat. Rev. Mol. Cell Biol.* 9:446–454.
10. Bornschlögl, T. 2013. How filopodia pull: what we know about the mechanics and dynamics of filopodia. *Cytoskeleton.* 70:590–603.
11. Van Goor, D., C. Hyland, …, P. Forscher. 2012. The role of actin turnover in retrograde Actin network flow in neuronal growth cones. *PLoS One.* 7:e30959.
12. Alieva, N. O., A. K. Efremov, …, A. D. Bershadsky. 2019. Myosin IIA and formin dependent mechanosensitivity of filopodia adhesion. *Nat. Commun.* 10:3593.
13. Kovar, D. R. 2007. Intracellular motility: myosin and tropomyosin in actin cable flow. *Curr. Biol.* 17:R244–R247.
14. Berg, J. S., and R. E. Cheney. 2002. Myosin-X is an unconventional myosin that undergoes intrafilopodial motility. *Nat. Cell Biol.* 4:246–250. https://doi.org/10.1038/ncb762.
15. Arjonen, A., R. Kaukonen, and J. Ivaska. 2011. Filopodia and adhesion in cancer cell motility. *Cell Adh. Migr.* 5:421–430.
16. Lagarrigue, F., P. Vikas Anekal, …, M. H. Ginsberg. 2015. A RIAM/lamellipodin–talin–integrin complex forms the tip of sticky fingers that guide cell migration. *Nat. Commun.* 6:8492.
17. Miihkinen, M., M. L. B. Grönloh, …, G. Jacquemet. 2021. Myosin-X and talin modulate integrin activity at filopodia tips. *Cell Rep.* 36:109716.
18. Bouvard, D., J. Pouwels, …, J. Ivaska. 2013. Integrin inactivators: balancing cellular functions in vitro and in vivo. *Nat. Rev. Mol. Cell Biol.* 14:430–442.
19. Kong, F., A. J. García, …, C. Zhu. 2009. Demonstration of catch bonds between an integrin and its ligand. *J. Cell Biol.* 185:1275–1284. https://doi.org/10.1083/jcb.200810002.
20. Sun, Z., M. Costell, and R. Fässler. 2019. Integrin activation by talin, kindlin and mechanical forces. *Nat. Cell Biol.* 21:25–31.
21. Yao, M., B. T. Goult, …, J. Yan. 2016. The mechanical response of talin. *Nat. Commun.* 7:11966.
22. Hawk, C. S., C. Coelho, …, A. Casadevall. 2019. Integrin β1 promotes the interaction of murine IgG3 with effector cells. *J. Immunol.* 202:2782–2794.
23. Kress, H., E. H. K. Stelzer, …, A. Rohrbach. 2005. Control of relative radiation pressure in optical traps: application to phagocytic membrane binding studies. *Phys. Rev. E Stat. Nonlin. Soft Matter Phys.* 71:061927.
24. Owen, L. M., N. A. Bax, …, A. R. Dunn. 2022. The C-terminal actin-binding domain of talin forms an asymmetric catch bond with F-actin. *Proc. Natl. Acad. Sci. USA.* 119. e2109329119.
25. Schwarz, U. S., T. Erdmann, and I. B. Bischofs. 2006. Focal adhesions as mechanosensors: the two-spring model. *Biosystems.* 83:225–232.
26. Novikova, E. A., and C. Storm. 2013. Contractile fibers and catch-bond clusters: a biological force sensor? *Biophys. J.* 105:1336–1345.
27. Erdmann, T., and U. S. Schwarz. 2012. Stochastic force generation by small ensembles of myosin II motors. *Phys. Rev. Lett.* 108:188101.

28. Gillespie, D. T. 1977. Exact stochastic simulation of coupled chemical reactions. *J. Phys. Chem.* 81:2340–2361.

29. Changede, R., and M. Sheetz. 2017. Integrin and cadherin clusters: a robust way to organize adhesions for cell mechanics. *Bioessays.* 39:1–12.

30. Zhang, H., J. S. Berg, …, S. Strömblad. 2004. Myosin-X provides a motor-based link between integrins and the cytoskeleton. *Nat. Cell Biol.* 6:523–531.

31. Mallavarapu, A., and T. Mitchison. 1999. Regulated actin cytoskeleton assembly at filopodium tips controls their extension and retraction. *J. Cell Biol.* 146:1097–1106.

32. Staiger, C. J., M. B. Sheahan, …, L. Blanchoin. 2009. Actin filament dynamics are dominated by rapid growth and severing activity in the Arabidopsis cortical array. *J. Cell Biol.* 184:269–280.

33. Roux, A., D. Cuvelier, …, B. Goud. 2005. Role of curvature and phase transition in lipid sorting and fission of membrane tubules. *EMBO J.* 24:1537–1545.

34. Baumgart, T., A. T. Hammond, …, W. W. Webb. 2007. Large-scale fluid/fluid phase separation of proteins and lipids in giant plasma membrane vesicles. *Proc. Natl. Acad. Sci. USA.* 104:3165–3170.

35. Römer, W., L.-L. Pontani, …, L. Johannes. 2010. Actin dynamics drive membrane reorganization and scission in clathrin-independent endocytosis. *Cell.* 140:540–553.

Biophysical Journal, Volume *121*

Supplemental information

Pulling, failing, and adaptive mechanotransduction of macrophage filopodia

Rebecca Michiels, Nicole Gensch, Birgit Erhard, and Alexander Rohrbach

SUPPLEMENTARY MATERIAL

S1. Force-dependence of bead velocity in optical trap

Analysis of pulling experiments against counteracting optical forces allows us to determine the force-dependency of the bead velocity v_{bd} (Figure S 1A). The optical forces, which we employ and for which we can determine the velocity, range from F_{opt} = 1 pN to approximately 30 pN. For forces smaller than 1 pN, displacements in our settings were so low that we could not determine a velocity reliably. We found an average velocity of approximately 50 pN. Interestingly, the bead velocity seems to be independent of the counteracting force in this range as depicted in Figure S 1B. This is remarkable, as we see considerably higher bead velocities for beads transported at F_{opt} = 0, where only the drag force in the range of 1fN to 1pN controls the velocity. Similar findings were presented by Kress et al.(1)

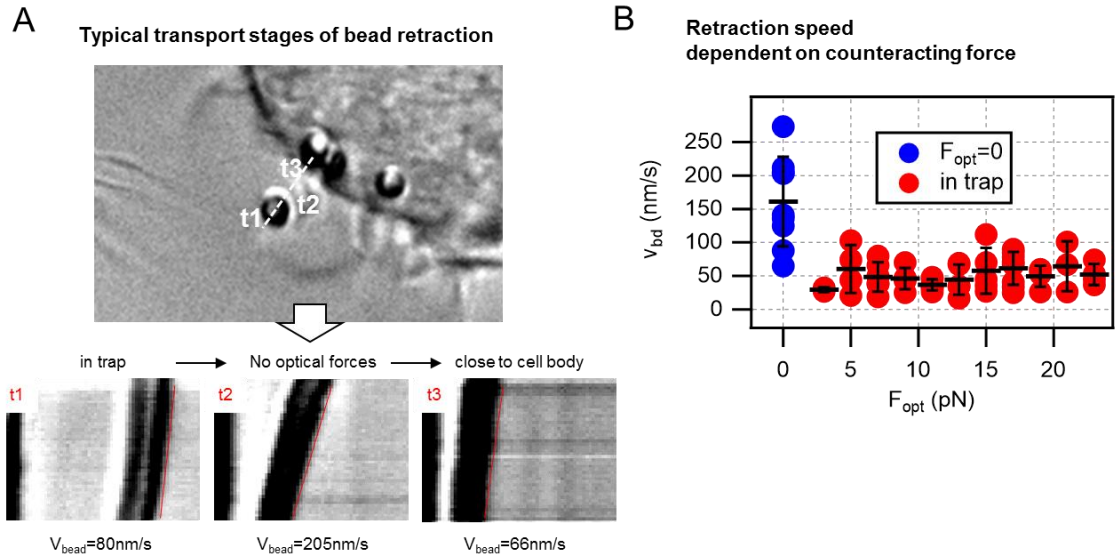

Figure S 1: Bead velocity in dependence of counteracting optical force from three independent experiments. A) brightfield images with 3 kymographs from different time points. B) Blue dots are derived from videotracking of freely pulled beads when the optical trap is switched off. Red dots are derived from particle tracking data of optically trapped beads.

Velocities of beads and eGFP speckles obtained from kymographs

Velocities from 1µm beads recorded in brightfield (DIC) mode and actin backbone speckles recorded in fluorescence mode are analyzed by lines placed manually along the edges of pronounced intensity variations in each two kymographs. An error of 10% is accepted by manually placing the lines as shown in the following five examples (10 kymographs).

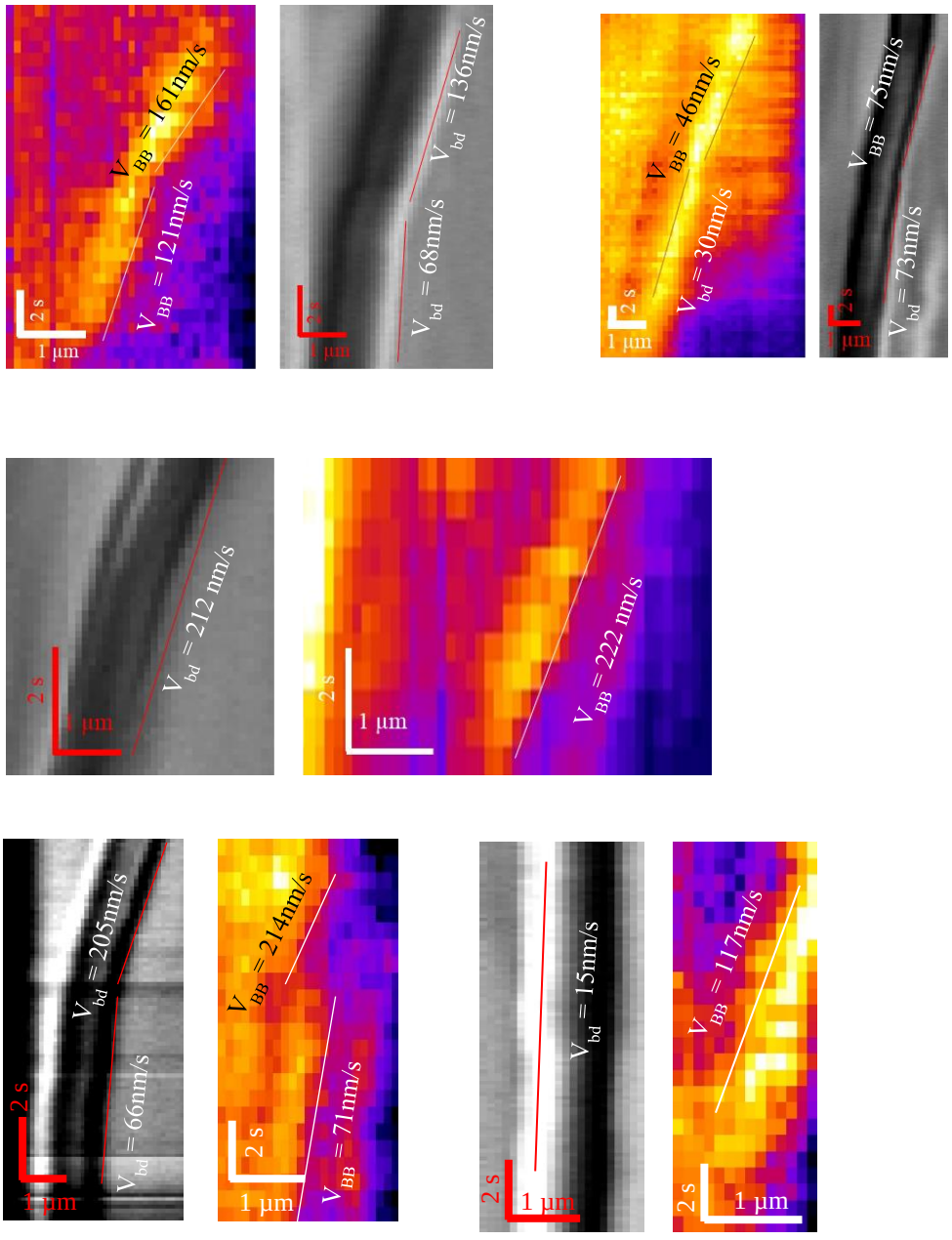

Figure S 2: Velocity analysis by kymographs, which have been recorded in parallel. Kymographs encoding bead velocities v_{bd} from brightfield images (shown in grayscale) and backbone velocities v_{BB} from fluorescent images (shown in fire scale). Pixel size is 103nm in horizontal direction for both cameras. Pixel size in vertical direction is 0.554 s for the fluorescent camera and 0.124 s for the brightfield camera.

S2. Influence of an external force on the extraction of fluctuation parameters.

During experiments the values for κ may rise strongly. As κ rises, the axis intercept AC(τ=0) of the autocorrelation function (AC) of the trajectory drops and the influence of external influences on the AC becomes more pronounced. In Figure S 3a a simulated retraction (blue curve; constant pulling velocity of 100 nm/s is assumed) is depicted alongside the simulated trajectory of a bead in a stationary trap (red). In both cases, the bead is confined in a very strong harmonic potential with κ = 0.5 pN/nm.
The stiffness parameter κ was calculated from the AC as described in Section 2. Figure S 3B left shows the stiffnesses over time for the displaced bead in blue and the undisturbed bead in red. The corresponding ACs are displayed on the right. It can be seen that a significant difference in κ arises if no correction is applied. This can be prevented by fitting the AC with an exponential with offset (Figure S 1C) or by pre-filtering data with a 400Hz highpass filter (Figure S 3D).

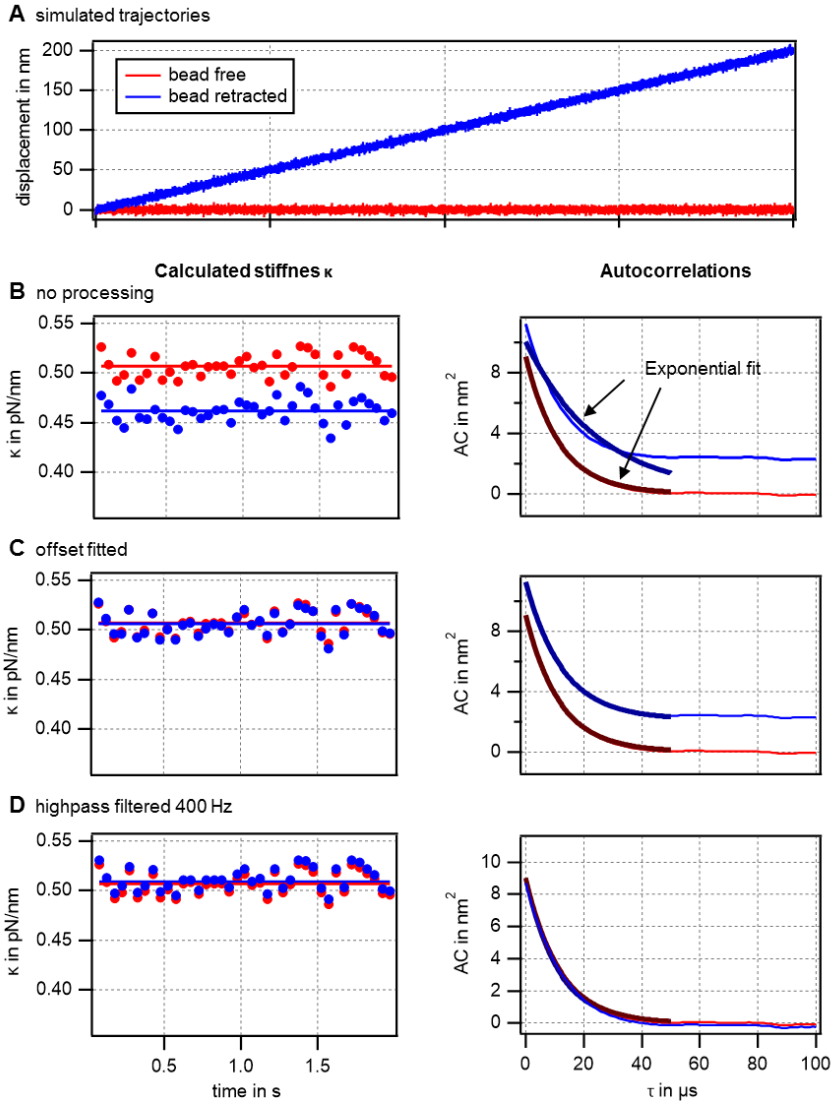

Figure S 3: Adjusting data evaluation can minimize the effects of external force on the calculated fluctuation parameters. In (A) the simulated trajectories for a pulled (blue) and for an undisturbed bead (red) in a stiff potential are shown. In (B),(C),(D) the stiffness parameter κ calculated for both sets (left) and the corresponding AC curves including the exponential fits (right) are shown. Dots in left graphs denote individual measurement points, lines the average values. The values in (B) are calculated using standard routine and the external movement causes significant distortion in AC and κ. This can be prevented by fitting an offset (C) or pre-filtering data (D).

S3. High-pass filtering bead position fluctuations

To find out to what extent external disturbances actually play a role in real data sets, a bead retraction curve was subjected to different forms of filtering before analysis. In Figure S 4A, the experimentally measured bead displacement is shown for one retraction event. In this case, the bead connects with the filopodium at around 5 s, a short pulling attempt is made, the attempt fails and the bead snaps back at 12 s, but the filopodium subsequently pulls again and is successful. In Figure S 4B, the calculated cellular stiffness parameter κ is depicted for the unprocessed data set (green curve, no HP) or highpass (HP) filtered with different corner frequencies (HP100 – HP800). Comparison of the stiffness curves κ before binding ($t < 5s$) shows that the highpass filtering leads to a small positive offset of κ when analyzing fluctuations of a free bead. The offset increases with increasing corner frequency. This is likely due to a small portion of the bead's fluctuations at lower frequencies being removed by the filtering. The constant offset does however not affect the shape of curves and the qualitative development of fluctuation parameters and is therefore not of great concern for biophysical analysis.

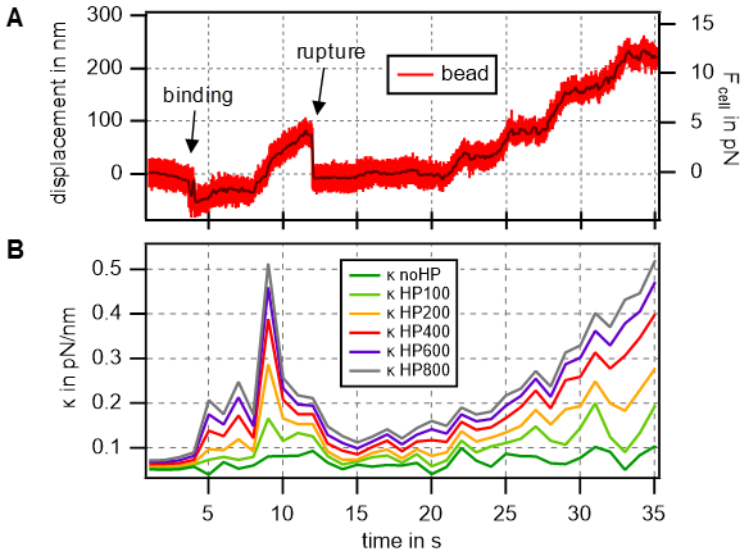

Figure S 4: Influence of highpass filtering on the calculated stiffness parameter κ. In (A) the bead retraction curve is shown and the timepoints of binding and a failure are indicated. The data was filtered with different corner frequencies (HP100 - HP800) before κ was calculated (B). Between 0 – 400 Hz filtering has a marked impact on curve shapes, while above 400 Hz only a small offset is added to κ with increasing filtering.

In the regime of 0 – 400 Hz, filtering does have a strong impact on the shape of the curves when the bead is connected to the cell. In the temporal development of κ derived from unprocessed data (green curve) neither the binding at $t = 3$ s nor the failure at $t = 12$ s lead to a notable change of cellular stiffness parameter κ. Intuitively this seems very unlikely from a biophysical point of view. These are the experimental situations where filtering is the greatest effect, since these changes not only lead to an offset, but to a completely different evolution of the fluctuation parameter κ.

It is likely that a significant amount of external movements caused by the cell occurs at frequencies below 400 Hz. The corner frequency of 400 Hz was therefore in the following used to pre-process fluctuation data. Intriguingly, the stages of the experiment where changes in filtered and unfiltered data are especially high are not necessarily associated with strong and fast cellular pulling.

S4. Development of κ_{mem} and F_{mem} in experiments with multiple failures

In some experiments we observed a series of several, subsequent failure events. In these cases we analyze how characteristic mechanical parameters change over the course of one pulling experiment. We observe for both the membrane holding force F_{mem} and the membrane stiffness κ_{mem} that parameters increase with the number of failures as depicted in Figure S 5A,B indicating that these physical parameters of the filopodium rise during pulling.

In conclusion, this is another observation supporting the assumption of a force-dependent adaptation of the filopodium. The rupture force F_{rup} rises only in some experiments with several failures, but not in general as depicted in Figure S 5C.

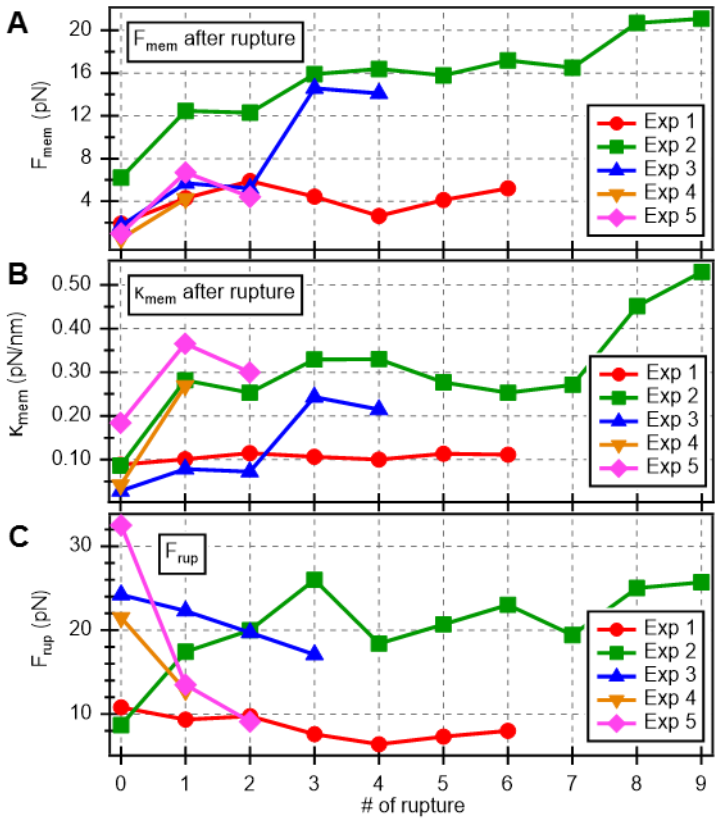

Figure S 5: Development of holding force F_{mem} (A) and stiffness κ_{mem} (B) during retraction for five independent experiments in which more than one rupture occurred. Both parameters show a tendency to increase with number of ruptures. (C) Development of rupture force during retraction for five independent experiments in which more than one rupture occurred. There is no overall tendency for the rupture force to increase with number of ruptures.

S5. Lifetime of actin-bead connection under force

From the observed failures we can derive an approximated lifetime of the bead-actin connection at the tip under force. Since pulling forces vary during experiments and we cannot control the loading rate, the results depicted in Figure S 6 can give only an estimate. The resulting force-dependent lifetime is calculated from the time that the cell pulls against force in a certain range, divided by the number of failures, which happen in this force range. At very low forces (< 5 pN) ruptures are unlikely and only very isolated events could be observed. We see a lifetime until failure of $\tau_{fail}(F) = 26.8 \pm 15$ s for forces F < 5 pN; a drop to rougly $\tau_{fail}(F) = 3$ s (see green arrow) in the range of F = 5-20 pN and a decrease to less than $\tau_{fail}(F) = 0.5$ s for forces F > 30 pN. Since the lifetime was calculated only from six experiments including failures, it represents a lower limit. Actual lifetimes may vary strongly from filopodium to filopodium, depending on the individual architecture and thickness of the filopodium. However, the quantiative coincidence between the numerial simulations is very good.

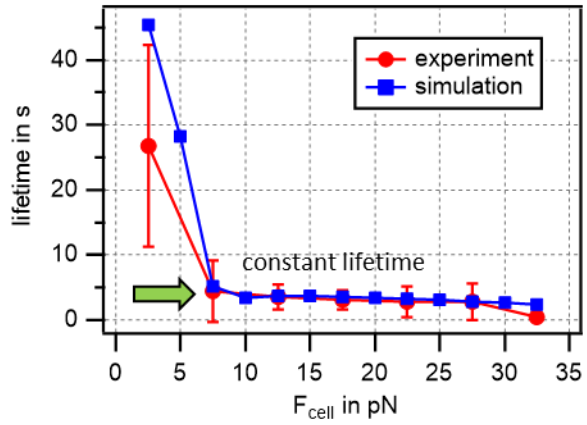

Figure S 6: Lifetime of actin-bead connection under force. The red markers represent measurement results derived from six independent experiments including failures. The blue markers indicate the lifetime of the simulated filopodia tips with catch bond clusters and membrane-actin connection.

S6. Exponential bead relaxation towards trap center after failures

When a failure happens, the bead snaps backwards towards the trap center in a rapid motion. Due to the high temporal resolution of the interferometric tracking, we can record these snap-backs in detail. When zooming in, an exponential relaxation of the bead towards the new holding position x_{hold} is visible (see Figure S 7). This movement can be fitted with an exponential function and the characteristic relaxation time constant τ_{rup} can be determined. The average τ_{rup} measured from 29 events is 37 ± 45 ms. The measured values show strong variations, but are all considerably longer than expected for a free bead in solution . The value is also considerably larger than the autocorrelation time τ_0, which is calculated from the fluctuation parameters and typically in the range of 100 µs. This indicates a strong damping of the snap back motion of the bead (because $\tau = \kappa/\gamma$ in the case of overdamped motion). We assume this to be the stretching of the membrane tube at filopodia tips during failures, which might be governed by the outflow of membrane lipids, which is a plastic rather than elastic deformation process (2).

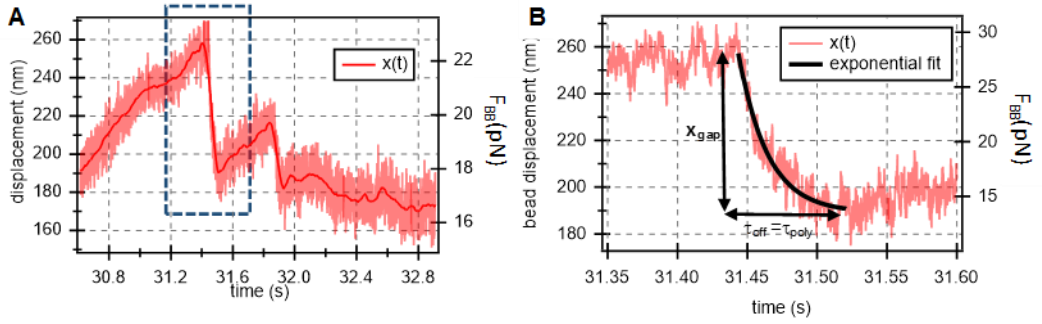

Figure S 7: A) 2s of backbone pulling is followed by a 0.1 s failure period. B) Movement of the bead during one failure event. The trajectory of the bead can be fitted linearily or by an exponential function as indicated by the black line.

S7. Relation between gap length, repolymerization speed and rupture force

A question that arises is how the overall snapback distance, i.e. the gap length $x_{gap} = \Delta x$ depend on the rupture force during experiments. Figure S 8A depicts the relationship between F_{rupt} and x_{gap} and shows that the the average snap-back distance remains constant during experiments and is independent of rupture force. Even as the rupture force increases, the amplitude of drops remains in the same range. This translates to an overall progress of the cell during pulling, as failures that happen at larger forces do not lead to a complete snap back of the bead.

Another parameter that rises (by almost a factor of two) with increased force at rupture is the tip velocity v_{tip}. The dependency of v_{tip} on F_{rupt} is depicted in Figure S 8B. An increase of the tip velocity means that the actin filament grows back faster after rupture of the actin-membrane connection. Consequently, it can catch up with the membrane and the attached bead in shorter time. Both do help the cell to fill the gap at the tip faster and resume pulling more quickly.

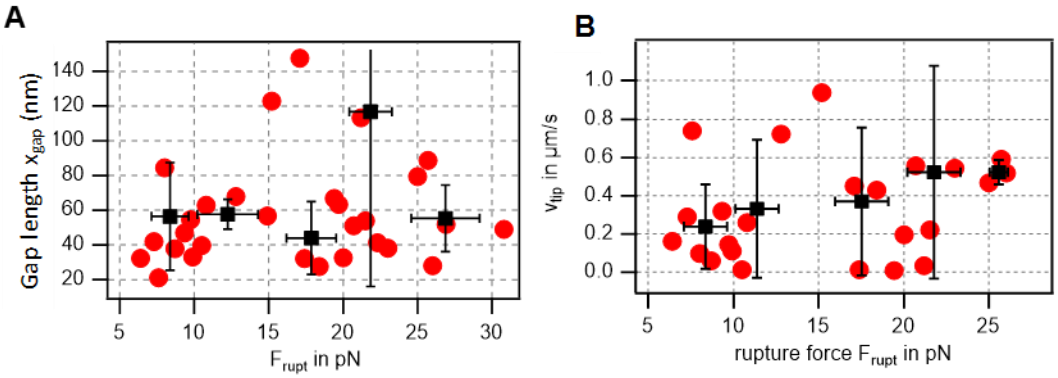

Figure S 8: A) Amplitude of the jump Δx in dependence of rupture force Frupt. Data shown is from seven independent pulling experiments in which one or several ruptures happened. A correlation between F_{rupt} and Δx cannot be determined. B) Tip velocity v_{tip} in dependence of rupture force F_{rup}. Shown are the raw data points (red) and the pooled data points (black).

S8. **Lifetime of a single catch-slip bond**

Catch(-Slip) bonds show a counterintuitive behavior as their lifetime initially increases under force. Under high forces stability decreases again, leading to a lifetime peak for individual bonds at a finite force. Catch bonds have been observed for many adhesion receptors including several isoforms of integrin receptors and bacterial adhesion molecules such as FimH(3-5)(3-5)[3-5].

Mathematically a two pathway model (in which unbinding is possible via two alternative pathways) describes catch bond characteristics. The catch path unbinding is opposed by application of force whereas the slip path unbinding is enhanced by force (6, 7). According to ref. (6), the force and temperature dependent unbinding rate for a single catch bond with catch and slip path characteristic length scales $\delta_c \approx \delta_s$ and zero force unbinding rates $k_{0,c}$, $k_{0,s}$ respectively can be expressed by

$$k_{off}(F) \approx k_0 \cdot \left(\exp\left(-(F+F_c)/F_0\right) + \exp\left((F+F_s)/F_0\right)\right) = 2k_0 \cdot \cosh\left(\frac{F+F_{\max}}{F_0}\right) \cdot \alpha^{-1} \quad \text{(S1)}$$

where $F_{\max} = (F_s + F_c)/2$ is the force at the maximal lifetime is indicated in Figure S 9. $k_{off}(F)$ is a catch-slip off-binding rate, which decreases for moderate forces and increases for stronger pulling forces. This behavior is typical for catch-(slip-) bonds such as integrins. Here, $F_0 = kT/\delta$ is a characteristic force corresponding to the (s)lip or (c)atch path length δ and $k_{off}(0) \approx k_0 \exp(-F_c/F_0) + k_0 \exp(F_s/F_0)$ is the zero-force rate (kT = thermal energy). At the force ½ (F_s+F_c), a single catch bond has a maximum life time $\tau_{on}(F) = 1/k_{off}(F)$.

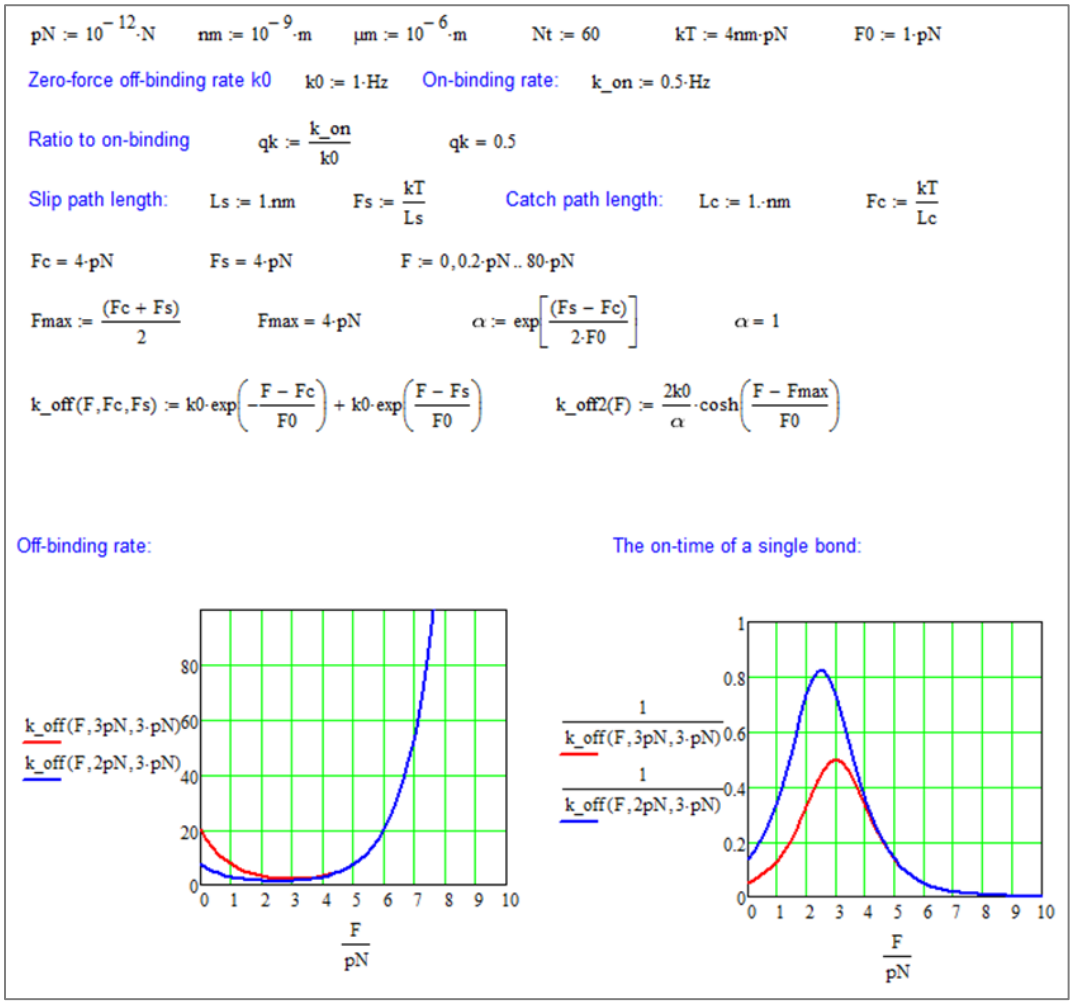

Figure S 9: A catch slip bond is characterized by and off-binding rate exponentially decreasing with pulling force plus an off-binding rate exponentially increasing with force. The inverse of this rate is the lifetime of the cluster, which shows the maximum at the force $F_{max} = (F_s + F_c)/2$, which is the average of the slip force and the catch force, which are based on a slip path length and catch path length of about 1 nm. In the example here, the slip force and the catch force are either 3 pN and3 pN (red curve) or 2 pN and 3 pN (blue curve).

Derivation of cosh(F) dependency of the off-binding rate of a single bond, which was used to calculate the plots in Fig. S8:

$$\begin{aligned} k_{off}(F) &= k_{0c} \cdot \exp(-F / F_{0c}) + k_{0s} \cdot \exp(F / F_{0s}) \\ &\approx k_0 \cdot \left(\exp\left(-(F + F_c)/F_0\right) + \exp\left((F + F_s)/F_0\right)\right) \\ &= k_0 \cdot \left(\exp\left(-(F - \tfrac{1}{2}(F_c + F_s))/F_0\right) + \exp\left(+(F - \tfrac{1}{2}(F_c + F_s))/F_0\right)\right) \cdot \exp\left(-\tfrac{1}{2}(F_c - F_s)/F_0\right) \\ &= 2k_0 \cdot \left(\cosh\left(\left(F - \tfrac{1}{2}(F_c + F_s)\right)/F_0\right)\right) \cdot \exp\left(-\tfrac{1}{2}(F_c - F_s)/F_0\right) \\ &= 2k_0 \cdot \left(\cosh\left((F - F_{max})/F\right)\right) \cdot \alpha^{-1} \end{aligned} \quad \text{(S2)}$$

S9. Slip bond and catch bond cluster under force

Slip bond clusters and catch bond clusters differ in their characteristic behaviour under force. The equilibrium condition of a cluster under a certain load is reached for the condition dN/dt= 0 for the cluster equation $\dot{N} = k_{on} \cdot (N_{tot} - N) - k_{off}(\frac{1}{N}F) \cdot N$. Due to stochastic variations, this is not on every timepoint the number of bonds, which are actually attached, but the number around which the cluster size will fluctuate at a given force. The number of attached bonds in the equilibrium condition, or the stable number of bonds, is termed N_s. For slip bond cluster, N_s drops under force, leading to a decrease in cluster size. This is depicted in Figure S 10A for a simulated slip bond cluster. In contrast, a catch bond cluster grows under force, reflected in an increase of the number N_s. This is depicted in Figure S 10B.

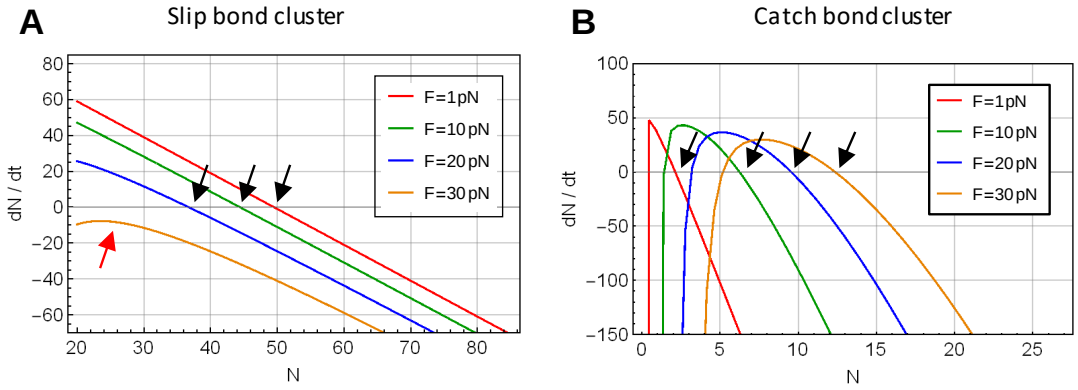

Figure S 10: (A) Characteristics of a cluster with a reservoir of Ntot = 100 slip bonds with kbT/ξ = 1 pN, k_0 = 1/s and k_{on} = 1/s under force. The force dependent change in number of attached bonds dN/dt is plotted versus the number of attached bonds N. The arrows mark the equilibrium condition. At higher forces the number of attached bonds N_s drops, at 30 pN a stable situation is not even possible anymore for this cluster. (B) Characteristics of a cluster with a reservoir of Ntot = 100 catch bonds with individual lifetime peak at 3.6 pN under force. The force dependent change in number of attached bonds dN/dt is plotted versus the number of attached bonds N. The left zero crossing of dN/dt is the unstable solution; the right zero point marked by the black arrows defines the stable solution N_s. The number N_s of bonds bound on average rises as load is increased.

S10. Lifetime of catch bond clusters depend on different variables

As described in the main text, the time between two ruptures (if observable) depends on various parameters among which the most important are the number of available bonds N_{tot} and the pulling force F. Here, we compare different cluster lifetimes for different unbinding rates k_{on} = 0.5 Hz and k_{on} = 1 Hz, as well as the the number N_s of bonds in the equilibrium situation, which was set by default to $N_s \approx N_{tot}/2$.

In the figure below, it can be seen that most of the parameters have an influence on the lifetime curves $\tau_{fail}(F)$, which is however not significant for the results discussed in the manuscript.

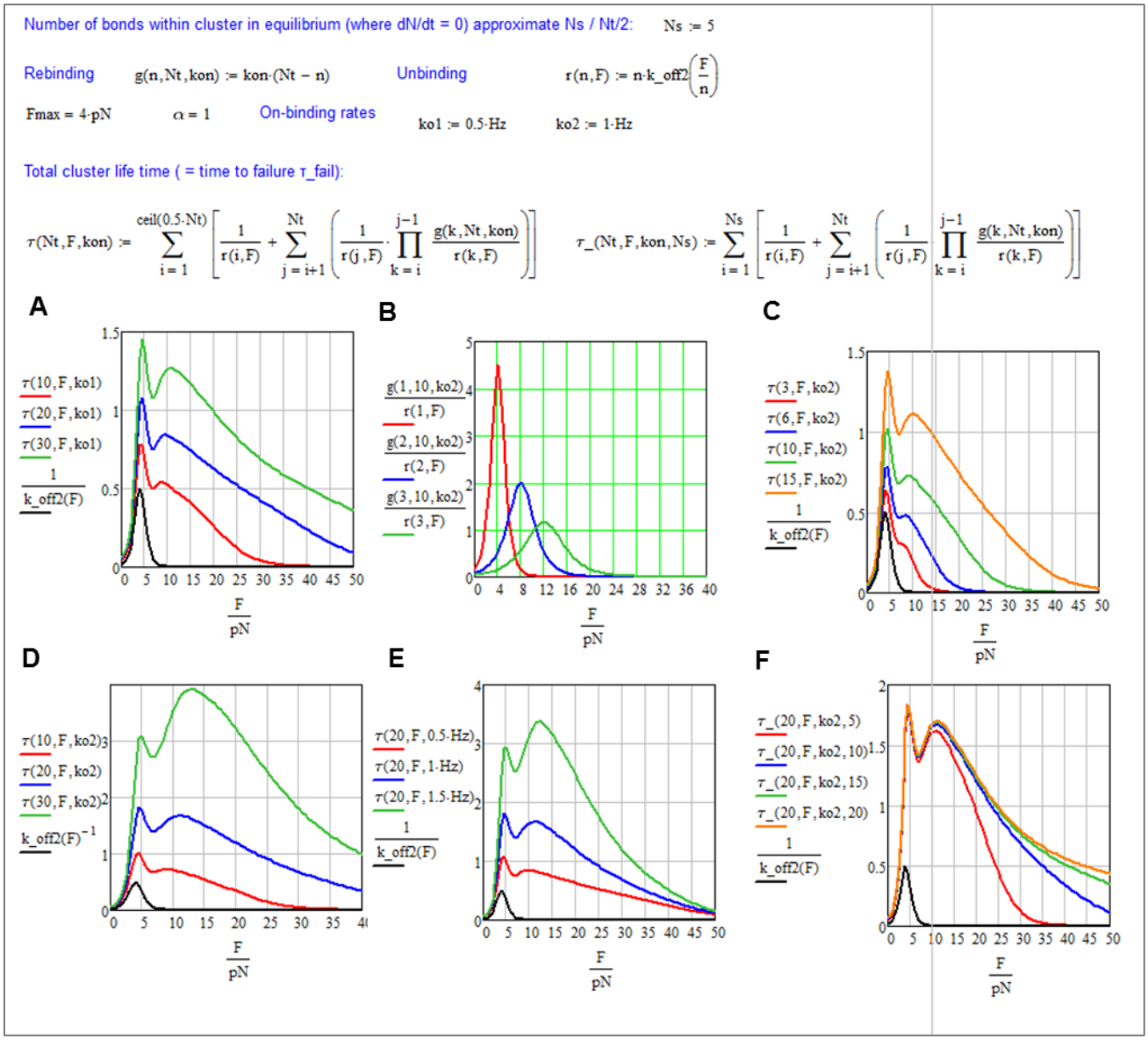

Figure S 11: (A,D) Lifetimes of catch bond clusters varying with force for different number of bonds (N_{tot} = 10,20,30) at two different on-binding rates. (B) Three different ratios g/r of rebinding to unbinding rates. (C) lifetimes of catch bond clusters varying with force for different different small bond numbers (N_{tot} = 3,6,10,15). (E) Cluster lifetime varying the force for N_{tot} = 20 at three different on-binding rates. (F) Cluster lifetime varying the force for N_{tot} = 20 at three different numbers of bonds in the equilibrium N_s = 5,10,15,20.

S11. Failing probability of a catch bond cluster as a function of time and pulling force

The probability p_{fail} that a cluster of N_{tot} available bonds fails (i.e. collapses) after a time t of continous pulling with force F is given by $p_{fail}(t, N_{tot}, F, k_{on}) = 1 - \exp\left(-t / \tau_{fail}(N_{tot}, F, k_{on})\right)$ (8) (9). Here, a higher on-binding rate leads to a slower increase of the failing probability. The probability 1-p_{fail} that the cluster holds over a time correspondingly is $p_{hold}(t, N_{tot}, F) = \exp\left(-t / \tau_{fail}(N_{tot}, F)\right)$.

Figure B shows that the probability that a bond cluster ruptures within τ_0 = 1s at low forces F < 4 pN hardly depends on the number of bonds N_{tot} or the on-binding rate k_{on}. On the one hand this shows that one failures and ruptures are likely at the beginning of pulling. On the other hand, it indicates that for pulling forces F > 4 pN the failing probability decreases significantly, such that efficient pulling of filopodia is possible for different numbers of bonds and on-binding rates, which cannot be measured experimentally.

Failure propability: $p\_fail(t, F, Nt, koff) := 1 - \exp\left(\frac{-t}{\tau(Nt, F, koff)}\right)$ $t := 0s, 0.1s .. 10s$

A

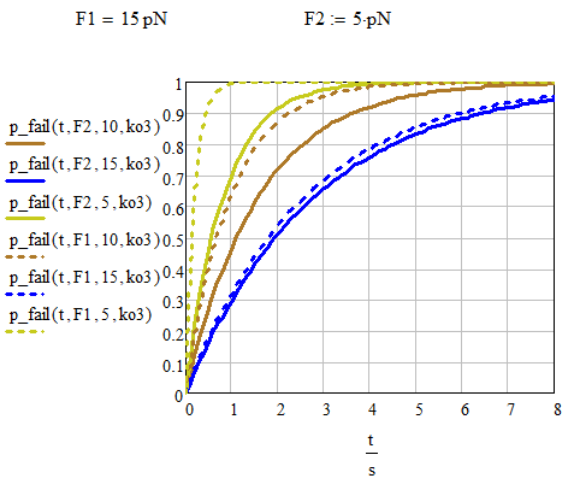

B

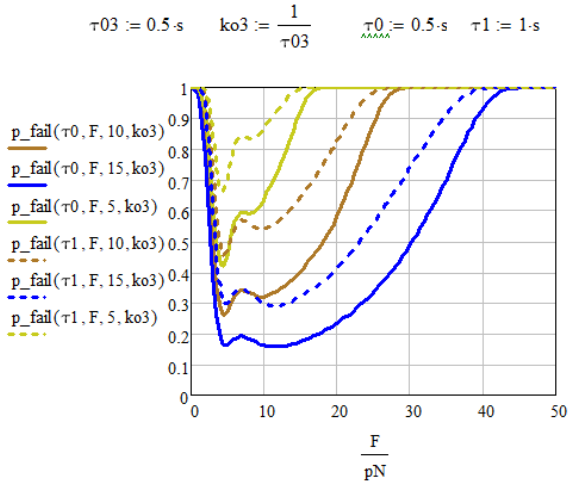

Figure S 12: (A) failure probability as a function of time for three different bond cluster sizes (N_{tot} = 10,20,30) and unbinding times k_{on} = 1 Hz and 0.5 Hz. The larger the bond cluster size and the higher the on-binding rate, the slower increases the failing probability. (B) Probability that a cluster of (N_{tot} = 10,20,30) bonds fails after τ_0 = 1s as a function of pulling force.

S12. Simple model for sawtooth like pulling and failing

The sawtooth like bead movement in Figure 5E consists of pulling periods and reconnection (repair) periods. In the first phase the bead is pulled at velocity $v_{BB} \cdot Q_T$ over the period $\tau_{fail}(F,N_{tot})$, i.e. the time between two ruptures (lifetime of bond cluster). A relatively fast snap back of the bead towards the trap center occurs at v_{BB}. Within a fraction of a second (period τ_{poly}) the bead drifts in rearward direction over some 10 nm (the distance x_{gap}), before the transport restarts.

The following calculation sets these two velocities and two periods into relation to investigate the overall displacement and the rupture frequency $k_{rup}(F,N_{tot}) = (\tau_{fail}+\tau_{poly})^{-1}$ for a situation where the pulling force is kept constant for some seconds. For simplicity the off-binding time τ_{poly} = 0.1s, the pulling velocity $v_{BB}/3$ and the tip velocity v_{tip} = 500nm/s are kept constant.

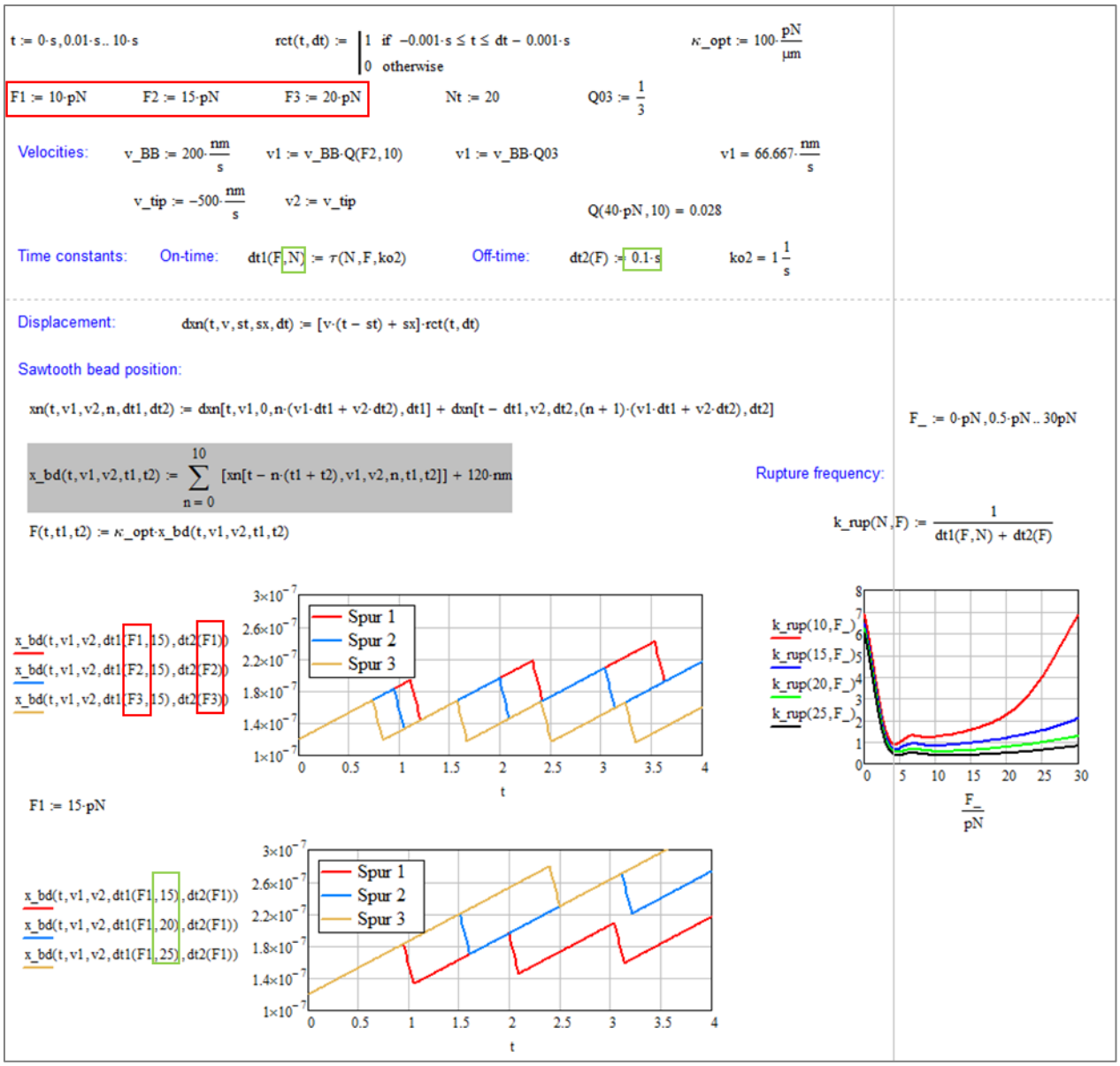

Figure S 13: Sawtooth like bead position changes indicating pulling and failing, which is characterized by the lifetime of the cluster, which varies with the pulling force and the number of available bonds. The rupture frequency is high (>5Hz) at low forces and remains approximately constant over a broad range of forces

S13. Adaptation and tip velocity

We have shown that especially three parameters improve during the course of one pulling experiment: These are the holding or membrane force F_{mem} and the corresponding displacement x_{hold} as well as the stiffness κ_{mem} of the filopodium after ruptures. In addition, there is a slight tendency for tip velocity v_{tip} to increase as rupture force increases (see Figure S 8B).

The velocity v_{tip} determines how long it takes the actin tip to polymerize back to the membrane and the bead at the tip of the membrane tube. If the actin tip caught up with the bead and the membrane before exponential relaxation has fully completed, this would decrease the jump amplitude x_{gap} and lead to an increase of the snap back position x_{hold} and consequently of F_{mem}. The numerical simulation shows however, that even a twofold increase of v_{tip} relative to the measured values does not have any impact on the snap back amplitude as depicted in Figure S 14 since the exponential relaxation of the bead is comparably much faster.

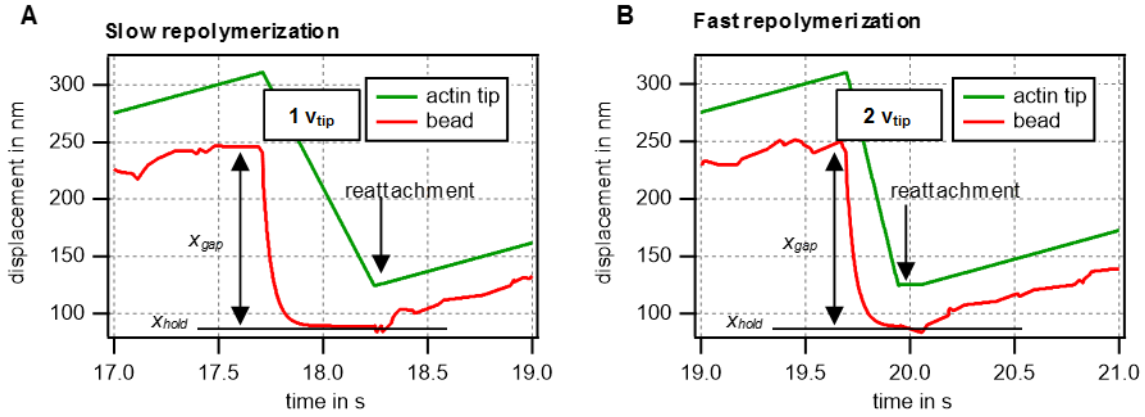

Figure S 14: Numerical simulation: Influence of the tip velocity v_{tip} *after rupture on jump amplitude (gap length)* x_{gap} *and final bead position* x_{hold}*. A twofold increase of* v_{tip} *does not influence the snap back of the bead. An arrow indicates the point at which the actin tip reconnects to the bead and membrane. The green curve of the actin tip and the red curve of the bead position do not overlap completely at his point since the spatial extension of adhesion proteins between is considered.*

S14. Model for overall retraction velocity and degree of adaptation (learning)

With an optimal pulling force an optimal overall retraction velocity $v_{mem}(F,N)$ can be achieved, which we call the optimal adaptation. Positions $x_{mem}(t)$ increases linearly with time with the average speed $v_{mem}(F,N)$, which is defined by pulling periods, reconnection periods and 2 velocities. For simplicity the off-binding time $\tau_{poly} = 0.1s$, the pulling velocity $v_{BB}/3$ and the tip velocity $v_{tip} = 500nm/s$ are kept constant.

$$\begin{aligned} v_{mem}(F,N) &= \frac{v_{bd}\cdot\tau_{on}(F,N)+v_{tip}\cdot\tau_{off}(F)}{\tau_{on}(F,N)+\tau_{off}(F)} \\ &= v_{bd}\cdot\frac{\tau_{on}(F,N)}{\tau_{tot}(F,N)} + v_{tip}\cdot\frac{\tau_{off}(F)}{\tau_{tot}(F,N)} \\ &= v_{bd}\cdot Q_{rup}(F,N) + v_{tip}\cdot(1-Q_{rup}(F,N)) = v_{tip} + Q_{rup}(F,N)\cdot\left(v_{bd}-v_{tip}\right) \\ &= dx_{mem}\,/\,\tau_{tot}(F,N) \end{aligned} \tag{S3}$$

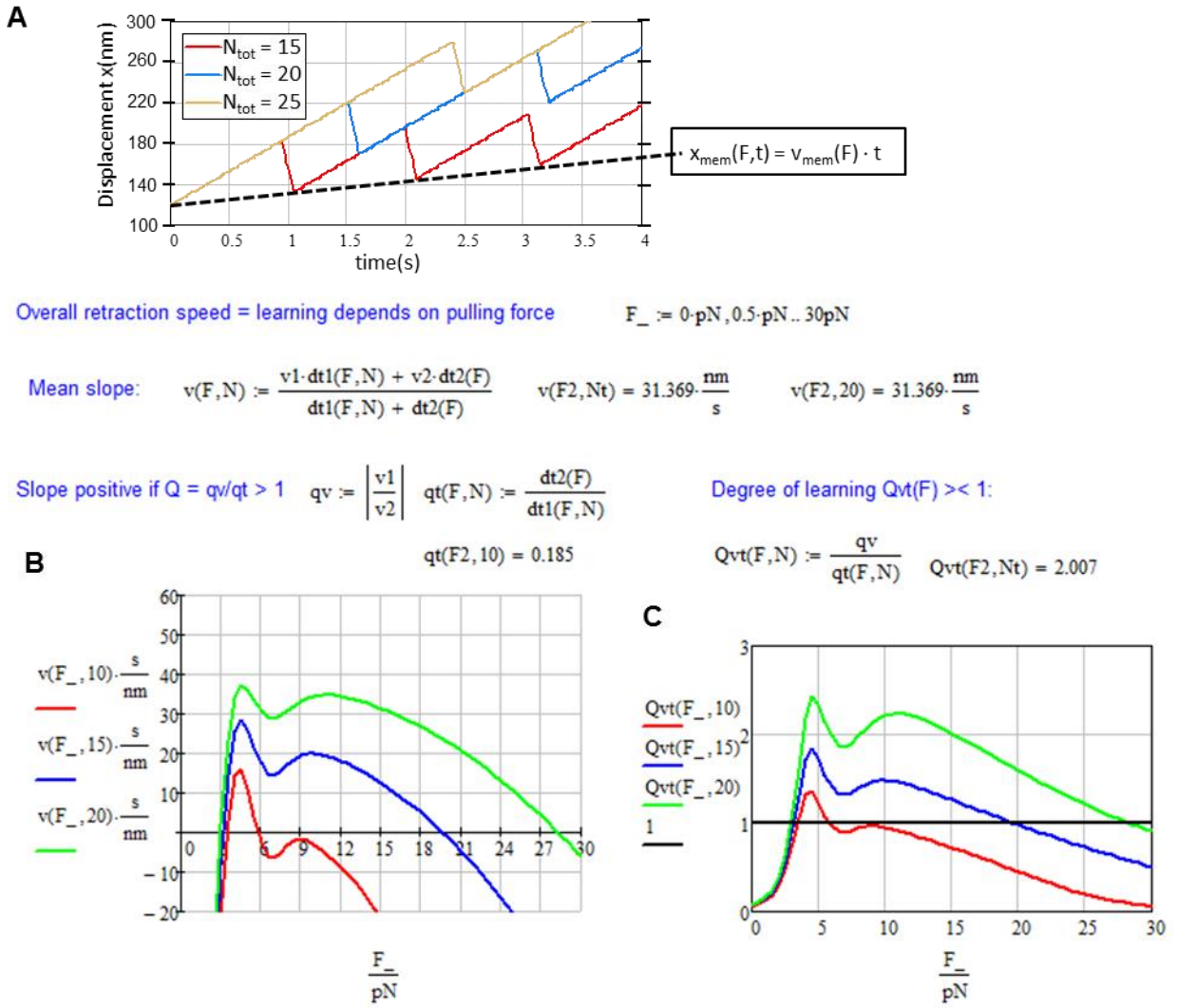

Figure S 15: (A) Positions $x_{mem}(t)$ increases linearly with time with the average speed $v_{mem}(F,N)$. (B) Overall retraction velocities as a function of pulling force for three different bond cluster sizes (N_{tot} = 10,15,20). (C) Degree Q_{vt} of adaptation (learning) as a function of pulling force for three different bond cluster sizes (N_{tot} = 10,15,20). The retraction towards the cell is given for $Q_{vt} > 1$.

S15. Numerical simulations filopodia pulling with slip bond cluster

Contrary to catch bond clusters, slip bond clusters generally decrease in size under load (10). The patterns of cluster growth (increased bond stiffness κ and friction γ) and intermittent failure events, which we observe experimentally, could not be reproduced accurately in simulations by assuming slip bond clusters (see Figure S 16). In a slip bond cluster the number of bonds will initially rise as binding is established, but drop quickly as pulling continues and load is increased (Figure S 16a,b). The cluster is driven subsequently and rapidly into an unstable regime and collapes (failure). When averaging the overall bond stiffness and viscosity over many attempts, we see an initial increase in bond stiffnes κ and friciton γ, which results from the initial binding phase. However, as force further increases, both parameters start to drop again (Figure S 16c,d).

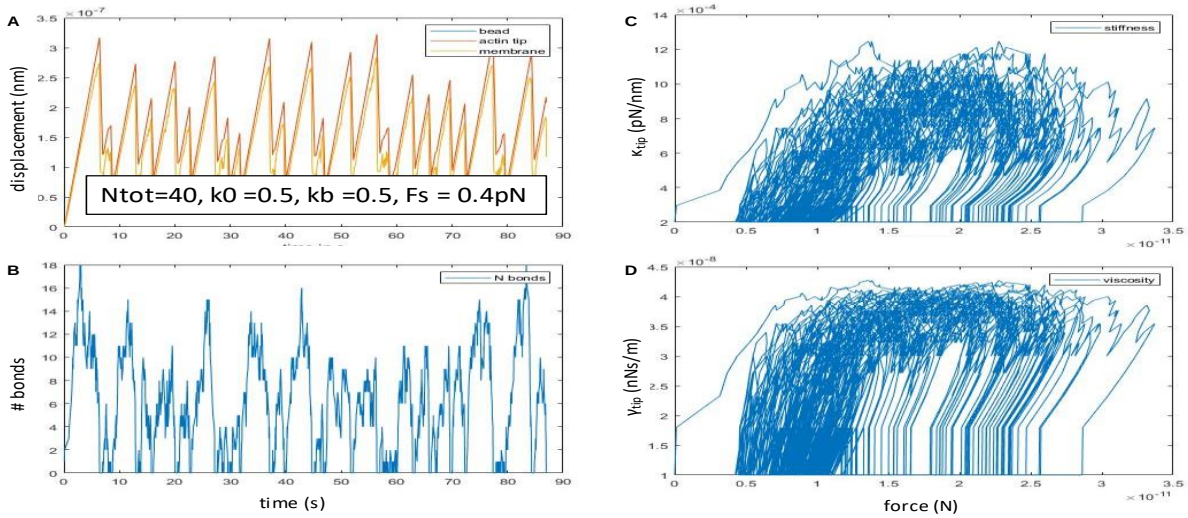

Figure S 16: Simulated filopodia retraction assuming a slip bond cluster. A) Simulated trajectory of the bead with multiple failures. B) Number of attached bonds during pulling. While the number increases initially for each rebinding event, it drops quickly again under load. C),D) Averaged dependence of bond stiffness κ and friction γ on counteracting force. While an initial rise is visible (due to re-establishment of cluster after failures), both parameters drop again as load increases.

S16. Table of measured failure parameters

Table S 1: Parameters measured in 30 analyzed failure events from filopodia retraction attempts.

event #	F_{rup} (pN)	F_{mem} (pN)	ΔF (pN)	Δκ (pN/µm)	κ_{mem} (pN/µm)	τ_{rup} (s)	τ_0 (s)	τ_{off} (s)
1	8.7	6.2	2.47	0.106	8.6e-02	0.026	8.8e-05	0.47
2	17.4	12.47	4.9	0.276	0.282	0.2	6e-05	3.77
3	20	12.3	7.6	0.237	0.253	0.178	7.8e-05	0.429
4	26	15.9	10.2	0.649	0.329	0.06565	4.3e-05	0.219
5	18.4	16.4	1.9	-	0.33	0.011	6.9e-05	0.049
6	20.7	15.8	4.85	0.185	0.277	0.0477	7.7e-05	0.0969
7	23	17.2	5.7	0.351	0.253	0.047	7.5e-05	0.1169
8	19.4	16.5	2.9	0.09.7	0.271	0.02	7.1e-05	4.4115
9	25	20.7	4.4	0.442	0.452	0.0261	6.1e-05	0.105
10	25.7	21.1	4.66	0.639	0.53	0.0175	5.9e-05	0.0877
11	15.2	8.95	6.28	0.346	0.24	0.0072	6e-05	0.067
12	9.9	2.2	7.75	0.731	0.634	0.023	5e-05	0.61
13	10.8	1.9	8.86	0.1137	8.8e-02	0.065	7.5e-05	0.34
14	9.34	4.3	5.1	0.9	0.101	0.015	6.8e-05	0.159
15	9.75	5.9	3.8	0.065	0.115	0.0029	7.1e-05	0.265
16	7.6	4.42	3.25	0.061	0.106	0.041	7e-05	0.044
17	6.4	2.61	3.77	5.5e-02	9.98e-02	0.0145	6.7e-05	0.235
18	7.3	4.12	3.2	2.6e-02	0.113	0.0174	7.2e-05	0.11
19	8	5.2	2.79	4.4e-02	0.111	0.0049	8.1e-05	0.279
20	21.5	0.5	21	0.783	4.1e-02	0.0062	0.00099	1.35
21	12.8	4.23	8.6	9.1e-02	0.269	0.027	6e-05	0.17
22	24.2	14.6	9.6	2.481	0.243	0.0076	6.1e-05	0.094
23	22.3	19.6	2.68	1.18	0.382	0.045	7.1e-05	-
24	19.7	16.9	2.72	0.213	0.309	0.051	7e-05	-
25	17.1	14.1	3.05	6.3e-02	0.215	0.0056	7.2e-05	0.104
26	30.8	26.8	3.97	0.265	0.71	0.045	6.7e-05	-
27	26.9	21.2	5.66	-	0.69	0.0043	7.7e-05	-
28	21.2	14.4	6.79	0.22	0.49	0.066	1e-05	1.94
29	14.9	11.6	3.3	-	0.581	0.027	8.3e-05	-
30	10.5	2.54	7.93	0.372	9.97e-02	0.00035	0.000158	6.22
Average	17.02 ± 6.98	11.36 ± 7.24	5.66 ± 3.72	0.407 ± 0.52	0.290 ± 0.192	0.0372 ± 0.0459	1.01e-04 ± 1.67e-04	0.867 ± 1.585

S17. Parameters used for the simulation

The parameters used for the stochastic gillespie simulation of a clatch bond cluster at filopodia tips shown in Figure 7 of the paper are listed below.

v_{BB}= 50 nm/s
v_{poly} = 400 nm/s
κ_{opt} = 100 pN/µm
κ_{mem} = 200 pN/µm
γ_{mem} = 10 pN·ms/µm = 10nN·s/m
κ_{rec} = 250 pN/µm
γ_{rec} = 40 pN·ms/µm
κ_{link} = 100 pN/µm
γ_{link} = 10 pN·ms/µm
N_{tot} = 40
F_c = 4.5 pN
F_s=4.6 pN
k_0=0.5

The total number of bonds N_{tot} was set to 40. This is a realistic value assuming that the membrane coats the bead by an area of around 0.2· µm² and taking a receptor spacing corresponding to the spacing of integrins found in focal adhesions of around 50 - 100 nm (11)

The values that are used to model κ_{rec}, κ_{mem} and κ_{link} can be compared to those of molecules for which values can be found in existing literature. However, such data is at present sparse. There exist some reported values for the stiffness of integrin or talin molecules mostly having been obtained using AFM force spectroscopy measurements. Here the receptor stiffness is chosen as κ_{rec} = 250 pN/µm. The value corresponds to an average number of five receptors with a stiffness of individual receptors of 50 pN/µm. The stiffness parameter set for the linker is κ_{link} = 100 pN/µm γ_{link} = 10 pN·ms/µm according toour measuremnts. These values lie within the reported range of elasticities for integrin and talin (12-14). The membrane stiffness parameter κ_{mem} = 200 pN/µm and γ_{mem} = 10 pN·ms/µm were estimated from the conducted measurements.

Although we have choesen the most probable and reliable parameters according to literature and our own measurements, there can be other sets of parameters that allow to reproduce the experimental results at least partially. Once the exact molecular composition of the bond is known the model can be refined by using more precise input parameters. Furthermore, in reality it is likely that the number of receptors N_{tot} also changes, which would additionally influence the behavior of the measured κ_{rec} and γ_{rec}.

At present, it is important to note that the dynamic building, enforcement and sudden instability of the tip connection in principle can be remodeled accurately by assuming a catch bond cluster, linking the actin BB to the bead.

References

1. Kress, H., E. H. K. Stelzer, D. Holzer, F. Buss, G. Griffiths, and A. Rohrbach. 2007. Filopodia act as phagocytic tentacles and pull with discrete steps and a load-dependent velocity. Proc. Natl. Acad. Sci. U. S. A. 104(28):11633-11638. Article.
2. Raucher, D., and M. P. Sheetz. 1999. Characteristics of a Membrane Reservoir Buffering Membrane Tension. Biophysical Journal 77(4):1992-2002.
3. Sokurenko, E. V., V. Vogel, and W. E. Thomas. 2008. Catch bond mechanism of force-enhanced adhesion: counter-intuitive, elusive but … widespread? Cell Host & Microbe 4(4):314-323.
4. Kong, F., A. J. García, A. P. Mould, M. J. Humphries, and C. Zhu. 2009. Demonstration of catch bonds between an integrin and its ligand. The Journal of Cell Biology 185(7):1275. 10.1083/jcb.200810002.
5. Sauer, M. M., R. P. Jakob, J. Eras, S. Baday, D. Eriş, G. Navarra, S. Bernèche, B. Ernst, T. Maier, and R. Glockshuber. 2016. Catch-bond mechanism of the bacterial adhesin FimH. Nature Communications 7:10738. Article.
6. Novikova, Elizaveta A., and C. Storm. 2013. Contractile Fibers and Catch-Bond Clusters: a Biological Force Sensor? Biophysical Journal 105(6):1336-1345.
7. Pereverzev, Y. V., O. V. Prezhdo, M. Forero, E. V. Sokurenko, and W. E. Thomas. 2005. The Two-Pathway Model for the Catch-Slip Transition in Biological Adhesion. Biophysical Journal 89(3):1446-1454.
8. Collins, D. H., and R. L. Warr. 2019. Failure time distributions for complex equipment. Quality and Reliability Engineering International 35(1):146-154.

9. Rausand, M., and A. Høyland. 2003. System Reliability Theory: Models, Statistical Methods, and Applications, 2nd Edition. Wiley, Hoboken, NJ.
10. Novikova, E., and C. Storm. 2019. Evolving roles and dynamics for catch and slip bonds during adhesion cluster maturation.
11. Changede, R., and M. Sheetz. 2017. Integrin and cadherin clusters: A robust way to organize adhesions for cell mechanics. BioEssays 39(1):e201600123.
12. Yao, M. X., B. T. Goult, H. Chen, P. W. Cong, M. P. Sheetz, and J. Yan. 2014. Mechanical activation of vinculin binding to talin locks talin in an unfolded conformation. Sci Rep-Uk 4.
13. Yao, M. X., B. T. Goult, B. Klapholz, X. Hu, C. P. Toseland, Y. J. Guo, P. W. Cong, M. P. Sheetz, and J. Yan. 2016. The mechanical response of talin. Nature Communications 7.
14. Chen, Y. F., H. Lee, H. B. Tong, M. Schwartz, and C. Zhu. 2017. Force regulated conformational change of integrin alpha(v)beta(3). Matrix Biol 60-61:70-85.